

# Unravelling the high-altitude Nansen blue ice field meteorite trap (East Antarctica) and implications for regional palaeo-conditions

Harry Zekollari<sup>a,b,c,\*</sup>, Steven Goderis<sup>a</sup>, Vinciane Debaille<sup>d</sup>,  
Matthias van Ginneken<sup>a,d,e</sup>, Jérôme Gattacceca<sup>f</sup>, ASTER Team<sup>1</sup>, A.J. Timothy Jull<sup>g</sup>,  
Jan T.M. Lenaerts<sup>h</sup>, Akira Yamaguchi<sup>i,j</sup>, Philippe Huybrechts<sup>a</sup>, Philippe Claeys<sup>a</sup>

<sup>a</sup> Earth System Science, Vrije Universiteit Brussel, Brussels, Belgium

<sup>b</sup> Laboratory of Hydraulics, Hydrology and Glaciology (VAW), ETH Zürich, Zürich, Switzerland

<sup>c</sup> Swiss Federal Institute for Forest, Snow and Landscape Research (WSL), Birmensdorf, Switzerland

<sup>d</sup> Laboratoire G-Time, Université Libre de Bruxelles, Brussels, Belgium

<sup>e</sup> Geological Survey of Belgium, Royal Belgian Institute of Natural Sciences, Brussels, Belgium

<sup>f</sup> Aix Marseille Univ, CNRS, IRD, Coll France, CEREGE, Aix-en-Provence, France

<sup>g</sup> Department of Geosciences, University of Arizona, Tucson, AZ, United States

<sup>h</sup> Department of Atmospheric and Oceanic Sciences, University of Colorado Boulder, Boulder, United States

<sup>i</sup> National Institute of Polar Research, Tokyo, Japan

<sup>j</sup> The Graduate University for Advanced Studies (SOKENDAI), Tokyo, Japan

Received 19 March 2018; accepted in revised form 23 December 2018; available online 4 January 2019

## Abstract

Antarctic blue ice zones, the most productive locations for meteorite recovery on Earth, contain old ice that is easily accessible and available in large quantities. However, the mechanisms behind these meteorite traps remain a topic of ongoing debate. Here, we propose an interdisciplinary approach to improve our understanding of a meteorite trap in Dronning Maud Land (East Antarctica) on the Nansen blue ice field meteorite trap (2600–3100 m above sea level), where more than half of the Asuka meteorites have been collected. Based on 185 surface blue ice samples, one of the largest observed spatial patterns in oxygen isotopic variation to date is found. Relying on meteorites for which the terrestrial ages are determined using <sup>14</sup>C and <sup>36</sup>Cl, this surface ice is interpreted to date from the Last Interglacial up to the present-day. By combining state-of-the-art satellite derived surface velocities, surface mass balance modelling and ice flow modelling, we estimate that about 75–85% of the meteorites found on the ice field were supplied by ice flow after entering the ice sheet in an accumulation area of a few hundred square kilometres located south (upstream) of the ice field. Less than 0.4 new meteorites per year are supplied to the ice field through ice flow, suggesting that the hundreds of meteorites found 25 years after the first visit to this ice field mostly represent meteorites that were previously not found, rather than newly supplied meteorites. By combining these findings, the infall rate of meteorites from space is estimated, which is in line with values from the literature, but situated at the higher end of the range. A comparison of the oxygen isotopic variation of the surface blue ice to that of the European Project for Ice Coring

\* Corresponding author at: Laboratory of Hydraulics, Hydrology and Glaciology (VAW), ETH Zürich, Zürich, Switzerland.  
E-mail address: [zharry@ethz.ch](mailto:zharry@ethz.ch) (H. Zekollari).

<sup>1</sup> ASTER Team: Georges Aumaitre, Didier L. Boulès, Karim Kedadouche.

in Antarctica (EPICA), Dronning Maud Land (EDML) ice core (located 750 km to the west, at the same elevation), suggests that the regional changes in topography have been relatively limited since the Last Interglacial, supporting theories of an overall stable East Antarctic Ice Sheet (EAIS) over this time period.

© 2019 Elsevier Ltd. All rights reserved.

**Keywords:** Antarctic meteorite trap; Nansen ice field; Terrestrial age; Stable isotope geochemistry; Satellite derived velocities; Palaeoclimate

## 1. INTRODUCTION

The Antarctic Ice Sheet is the most productive region for collecting meteorites on Earth (Cassidy et al., 1992; Harvey, 2003). Of all meteorites collected to date, more than 35,000 (ca. 65%) were retrieved on the Antarctic Ice Sheet (Meteoritical Bulletin Database, 2018). The high Antarctic meteorite recovery probability is mainly related to three factors. First, given the contrast between the typically dark, fusion crusted meteorites and the blue/white surroundings, they are visually easily detectable (Harvey et al., 2015). Secondly, due to the cold and dry conditions the meteorites are generally well-preserved and less susceptible to chemical and physical weathering compared to warmer environments (Shimizu et al., 1983; Koeberl and Cassidy, 1991; Scherer et al., 1997; Welten et al., 1997, 2008; Pourkhorsandi et al., 2017). Thirdly, and most importantly, blue ice areas on the Antarctic Ice Sheet can act as meteorite traps, or so called ‘meteorite stranding zones’ (e.g. Richter et al., 2015).

In these meteorite stranding zones, meteorites that fell inland, in the ice sheet’s accumulation area, are brought to the surface (Fig. 1a). This contrasts with the ordinary transport mechanism of meteorites, where they are moved to the edge of the ice sheet, before eventually being discharged into the ocean (Yoshida et al., 1971; Yanai, 1978; Whillans and Cassidy, 1983). In meteorite stranding zones, the upward-flowing ice, combined with surface ablation, leads to high concentrations of meteorites at the surface (Bintanja, 1999; Corti et al., 2003). Furthermore, low ice surface velocities can extend the residence time of meteorites at the surface and increase their local concentration. As a consequence, most meteorite recovery missions in the Antarctic focus on meteorite stranding zones (Delisle et al., 1993; Eppler, 2011; Herzog et al., 2015). Some meteorite stranding zones were subject to various studies and are relatively well understood (e.g. Nagata, 1982; Schultz et al., 1990; Folco et al., 2002, 2006; Corti et al., 2003; Welten et al., 2008; Spaulding et al., 2012). Other meteorite

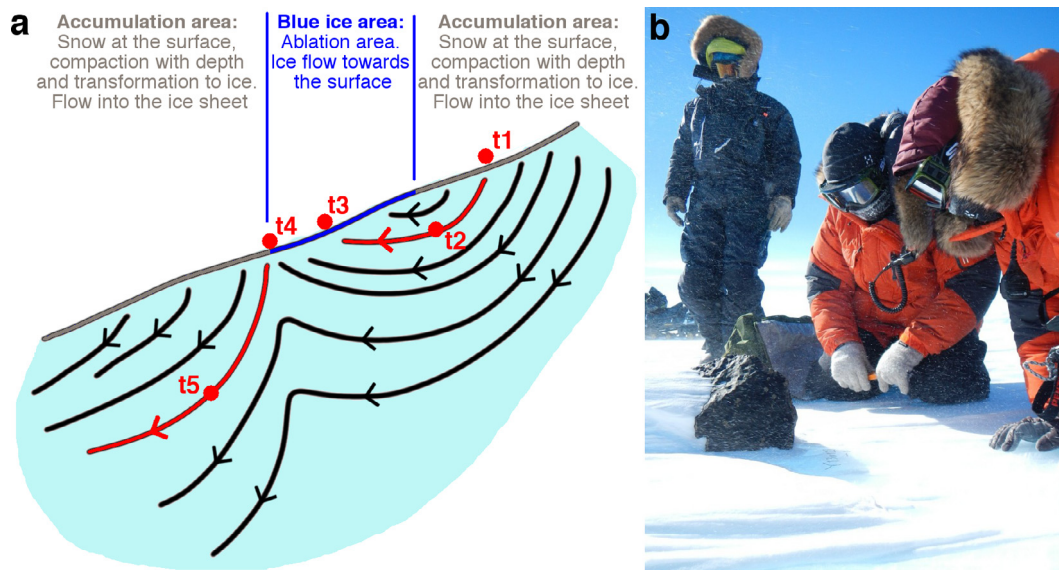


Fig. 1. (a) Schematic 2-D representation of mechanism behind meteorite trap. Transect view, in which the vertical dimension is exaggerated. The black lines are flow lines (arrows represent flow direction), while the red lines show a possible meteorite trajectory over time: t1: location where the meteorite reaches the surface and where it immediately enters the ice sheet (due to downward flow), t2: meteorite location while being transported within the ice sheet, t3: point where the meteorite reaches the surface (in blue ice area), t4: point until which the meteorite is transported at the surface of the blue ice area (through ice flow, potentially enhanced by katabatic winds); here, at the boundary of the blue ice area, the meteorite enters the ice sheet again (due to downward flow); t5: meteorite location while being transported further, until being forced back to the surface in a new ablation area, or until being discharged into the ocean. (b) Example of a meteorite collected on the Nansen blue ice field during the JARE-54/BELARE 2012–2013 expedition. This meteorite (A 12389), with a mass of 18 kg, is the largest meteorite retrieved on this ice field since its revisit in the 2010s. For more photographic material and expedition details, refer to Imae et al. (2015). (For interpretation of the references to colour in this figure legend, the reader is referred to the web version of this article.)

stranding zones, especially those located at high elevation, in terrain that is difficult to access, remain poorly understood and are the topic of ongoing debate (Sinisalo and Moore, 2010).

Blue ice areas are also interesting from a palaeoclimatic perspective (Bintanja, 1999; Corti et al., 2008; Sinisalo and Moore, 2010), as old ice is directly accessible at the surface (e.g. Spaulding et al., 2013). As a consequence, the sampling of ice is logistically and financially far less demanding compared to the classic deep drilling projects (e.g. Masson-Delmotte et al., 2011). Furthermore, blue ice areas have the potential to contain surface or shallow ice that is older than that recovered from deep drilling projects and can in some cases provide a higher temporal resolution (e.g. Sinisalo et al., 2007; Higgins et al., 2015; Bibby et al., 2016; Kehrl et al., 2018). Equally important, ice is available in large quantities, which is necessary for certain types of measurements, such as the characterization of trapped gasses and their isotopic composition (e.g. Sinisalo and Moore, 2010; Buizert et al., 2014). The main difficulty associated to using blue ice area records for palaeoclimatic purposes resides in the dating of the ice. This is more complex than in vertical drilling projects, where the ice age generally increases with depth. For surface blue ice dating, different techniques have been used and combined, including  $^{14}\text{C}$  dating of trapped air (e.g. Uglietti et al., 2016),  $^{81}\text{Kr}$  dating (e.g. Buizert et al., 2014),  $^{40}\text{Ar}$  dating (e.g. Higgins et al., 2015), radiometric dating of tephra layers found at the surface (e.g. Muhs et al., 1999; Curzio et al., 2008), cosmogenic dating of glacial tills (e.g. Bibby et al., 2016), dating by comparison to isotopic variations from ice cores through wiggle-matching (e.g. Moore et al., 2006) and constraining the terrestrial age from surface meteorites (e.g. Folco et al., 2006; Welten et al., 2006; Herzog et al., 2015).

In this study, through an interdisciplinary approach, we improve the current understanding of an Antarctic meteorite stranding zone located on the Nansen blue ice field (Dronning Maud Land, East Antarctica). By combining the oxygen isotopic composition ( $\delta^{18}\text{O}$ ) of the collected surface blue ice samples with the terrestrial age of selected meteorites, through ice flow and surface mass balance modelling, and by using a newly developed approach in which state-of-the-art satellite-derived surface velocities are combined with surface topographical information, we refine the mechanism behind the meteorite trap. This work also introduces new concepts that can be used to better characterize and understand other meteorite traps. Finally, we also discuss the implications of our findings for the past glaciological and climatological conditions of this region.

## 2. FIELD SITE AND CAMPAIGNS

The Nansen blue ice field (72°S 24°E, Dronning Maud Land) is located on the Antarctic plateau, about 100–120 km south of the Belgian Princess Elisabeth Station (see Fig. 2). Based on the spatial discontinuity of the ice patches, the blue ice field has been subdivided into Nansen A, Nansen B and Nansen C (Imae et al., 2015) (see Fig. 2). Nansen A is the lowest part of the ice field, with its western side at an elevation of about 2600 m above sea level (a.s.l.).

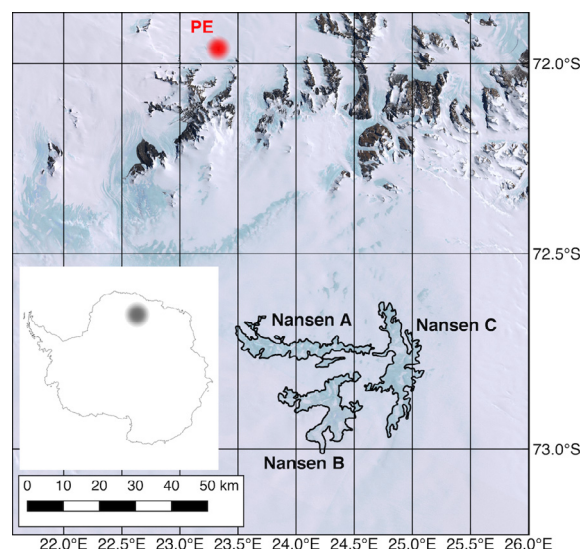


Fig. 2. Location of the Nansen Blue Ice Field and subdivision into Nansen A, Nansen B and Nansen C. The mountains in the north are the Sør Rondane Mountains. The location of the Princess Elisabeth Research Station (PE) is indicated with a red dot. Satellite images from the Landsat Image Mosaic of Antarctica (LIMA) (Bindschadler et al., 2008). The inset shows the position of the study area (black dot) in Antarctica. (For interpretation of the references to colour in this figure legend, the reader is referred to the web version of this article.)

Nansen C is the highest part of the ice field, with a surface elevation up to 3100 m a.s.l. in the southeast (see Fig. 3). The ablation over the ice field is governed by strong surface winds, promoting turbulence, latent heat release, and resulting sublimation, and is enhanced by the incoming solar radiation and low surface albedo, driving surface melting (see Appendix D and e.g. Bintanja, 1999; Lenaerts et al., 2017).

The ice field was first explored by the 29th Japanese Antarctic Research Expedition (JARE-29) (1987–1989), during which a total of 1582 meteorites were retrieved, of which 573 on Nansen A, 698 on Nansen B and 311 on Nansen C (Naraoka et al., 1990; Yanai et al., 1993). Nansen A was subsequently revisited during the austral summer of 2010–11 (Belgian Antarctic Research Expedition, BELARE 2010–2011), resulting in 218 newly collected meteorites (Goderis et al., 2011). Two years later, during the austral summer of 2012–13, a meteorite search expedition (JARE-54, BELARE 2012–2013) was organized on Nansen B and on the northern part of Nansen C (Debaille et al., 2013; Imae et al., 2013, 2015). During this expedition, 424 meteorites with a total weight of about 70 kg were collected, of which 368 on Nansen B, 55 on Nansen C and 1 on Nansen A (Fig. 4) (Imae et al., 2015) (Fig. 1b). With a total of more than 2200 collected meteorites, the Nansen ice field is one of the most productive meteorite collection sites in Antarctica: to date (September 2018), 6% of all Antarctic meteorites (ca. 60% of all meteorites labelled “Asuka”, named after the former Japanese Antarctic research station) have been collected on this ice field (Naraoka et al., 1990; Yanai et al., 1993; Goderis et al., 2011; Imae et al., 2015; Meteoritical Bulletin Database, 2018). Notice that given



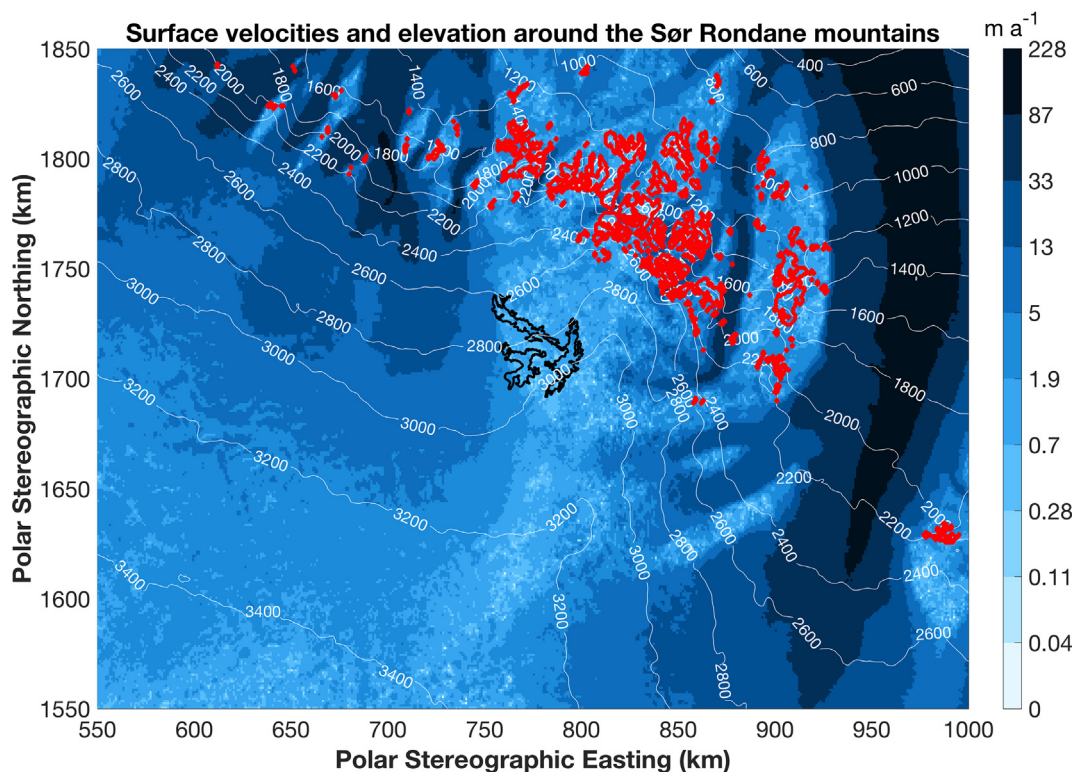


Fig. 3. Surface elevation (Fretwell et al., 2013) and satellite derived surface velocities (Mouginot et al., 2017; Rignot et al., 2017) around and south of the Sør Rondane Mountains (outlined in red). The white lines represent the surface elevation contours (in m a.s.l.), while the contours of the Nansen ice field are outlined in black. (For interpretation of the references to colour in this figure legend, the reader is referred to the web version of this article.)

the relatively low pairing for this ice field compared to other meteorite retrieval locations in Antarctica (see Section 6.2.2), and the fact that Antarctic meteorite numbers are commonly not corrected for pairing, the relative contribution from Nansen meteorites to the total number is probably higher.

During the 2012–13 expedition, 185 blue ice surface samples were collected, in addition to the meteorites (Figs. 4a and 5). The analyses and interpretations reported in this study are largely based on the meteorites and blue ice surface samples collected during this 2012–2013 campaign. Two moraines were also visited on Nansen B (see Fig. 5b for location), but only terrestrial rocks, which are entrained from the bedrock to the surface (e.g. Licht and Hemming, 2017; Graly et al., 2018), were found here (Jacobs et al., 2017). No meteorites and blue ice surface samples were collected in large areas of Nansen B (in the south and in the northeast; Fig. 4a) because these zones were only briefly (or not) visited due to the presence of a snow layer and/or crevasses (Imae et al., 2015). The crevasses make these areas difficult to access by snowmobiles, and potentially (strongly) reduce the number of meteorites at the surface.

### 3. ISOTOPIC SIGNAL OF BLUE ICE SURFACE SAMPLES

Blue ice surface samples were crushed and transported in sealed containers to the lab, where their isotopic compo-

sition was subsequently determined (at the AMGC stable isotope lab; see Appendix A. for details). A clear spatial pattern is observed in the oxygen isotopic composition ( $\delta^{18}\text{O}$ ) of the surface samples from Nansen B, with  $\delta^{18}\text{O} = [({}^{18}\text{O}/{}^{16}\text{O})_{\text{sample}}/({}^{18}\text{O}/{}^{16}\text{O})_{\text{ref}} - 1] \times 10^3$  (in ‰), relative to the Vienna Standard Mean Ocean Water (V-SMOW) (Fig. 5). To our knowledge, this is one of the largest observed spatial patterns in  $\delta^{18}\text{O}$  found to date in a blue ice area, with an extent of about 20 km (see e.g. Faure et al., 1993; Spaulding et al., 2013; Winter et al., 2016; with patterns along a horizontal scale of ca. 2 km, 5 km and 9 km, respectively). In the southern part of Nansen B, which will be referred to as Nansen B1 (Fig. 5a), the  $\delta^{18}\text{O}$  of the analysed samples typically varies between  $-48\text{‰}$  and  $-44\text{‰}$  ( $n = 46$ ) (see Appendix A for details). The Central part of the ice field (Nansen B2,  $n = 82$ ) is characterized by higher  $\delta^{18}\text{O}$  values, fluctuating between  $-42\text{‰}$  and  $-38\text{‰}$ . The northwestern part of the ice field (Nansen B3,  $n = 32$ ) has  $\delta^{18}\text{O}$  values in the same range as Nansen B1, varying between  $-48\text{‰}$  and  $-44\text{‰}$ . The surface samples collected in the northern part of Nansen C ( $n = 25$ ) range from  $-42\text{‰}$  to  $-36\text{‰}$  in  $\delta^{18}\text{O}$  (Fig. 5a).

### 4. TERRESTRIAL AGE OF METEORITES

The terrestrial age of a meteorite, defined as the time since its fall on Earth and consequent shielding from cosmic rays, can be used as a minimum estimate to constrain the

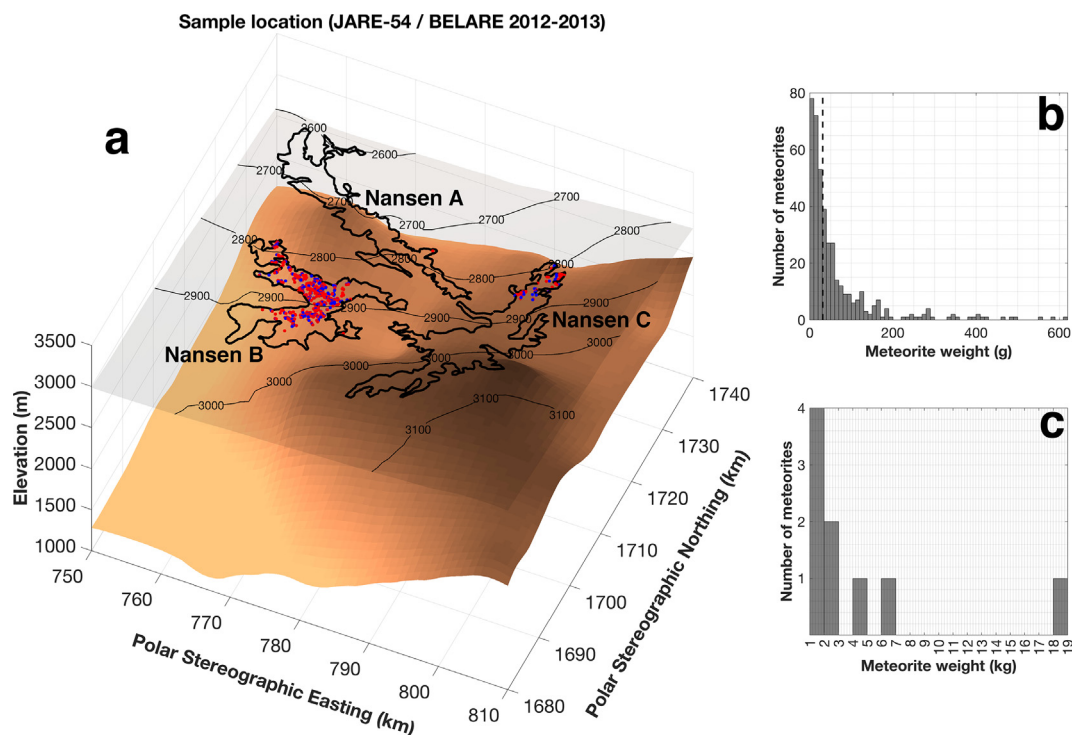


Fig. 4. (a) Sample locations of meteorites and blue ice samples collected on the Nansen ice field during the JARE-54/BELARE 2012–2013 expedition. The red dots represent the retrieval locations of the meteorites, while the blue dots represent the locations of the surface blue ice samples. The transparent surface is the surface elevation from the BEDMAP2 dataset (Fretwell et al., 2013), for which the 100-m contours are outlined. The bedrock elevation (brown surface) is also derived from the BEDMAP2 dataset. The thick black lines outline the Nansen ice field. Figure partly created with TopoZeko toolbox (Zekollari, 2017). (b and c) Mass distribution of all meteorites collected during the JARE-54/BELARE 2012–2013 expedition, with a mass between 0 and 620 g (10 g bins) (panel b) and a mass between 1 and 19 kg (1 kg bins) (panel c). Note that no meteorites were collected with a mass between 620 g and 1 kg. The vertical dotted line in panel b denotes the median mass of 31.3 g. (For interpretation of the references to colour in this figure legend, the reader is referred to the web version of this article.)

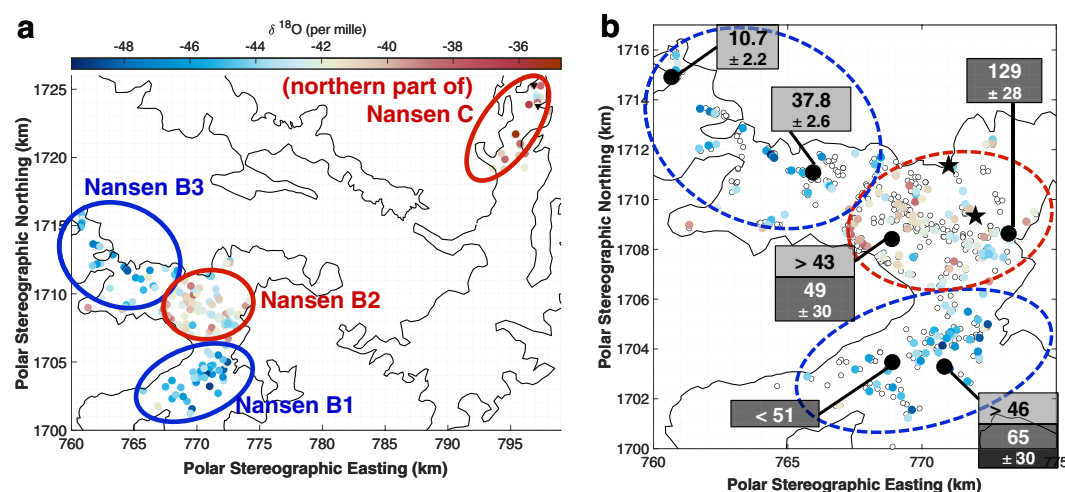


Fig. 5. (a)  $\delta^{18}\text{O}$  values of ice samples collected on Nansen blue ice field, (b)  $\delta^{18}\text{O}$  values of blue ice samples on the Nansen B ice field, together with the position and age of the dated meteorites from the JARE-54/BELARE2012–2013 expedition (Table 1). The small coloured dots represent the  $\delta^{18}\text{O}$  values of the surface blue ice samples, while the small circles represent the retrieval location of undated meteorites. The large black dots represent dated meteorites. The corresponding light grey boxes denote the terrestrial ages as determined by  $^{14}\text{C}$  dating, while the dark grey boxes correspond to the  $^{36}\text{Cl}$  dated terrestrial ages. The black lines represent the outlines of the ice fields. The black triangles (panel a) represent the location of the ash samples on Nansen C, while the black stars (panel b) represent the positions of the two moraines on Nansen B2. (For interpretation of the references to colour in this figure legend, the reader is referred to the web version of this article.)

Table 1  
Terrestrial age of selected meteorites collected on the Nansen blue ice field. For all new measurements, the technical details are summarized in [Appendix B](#).

Expedition	Meteorite	Mass (kg)	Classification	Longitude (°)	Latitude (°)	Dated terrestrial age (ka) and dating technique	Comment/reference
JARE-29 (Nansen A)	A 881371	0.01	Angrite	Nansen A (exact retrieval location unknown)		<60 ( <sup>81</sup> Kr)	<sup>81</sup> Kr dating by <a href="#">Weigel et al. (1997)</a> ; collected from western side of Nansen A
	A 881400	0.70	H3.8			21.2 ± 1.4 ( <sup>14</sup> C)	<sup>14</sup> C dating at Arizona AMS Lab ( <a href="#">Ninagawa et al., 2006</a> ); collected from western side of Nansen A
	A 881387	0.02	H3.8			16.7 ± 1.3 ( <sup>14</sup> C)	<sup>14</sup> C dating at Arizona AMS Lab ( <a href="#">Ninagawa et al., 2006</a> ); collected from western side of Nansen A
	A 881757	0.44	Lunar (gabbro)			60 ± 40 ( <sup>81</sup> Kr) <50 ( <sup>36</sup> Cl)	<sup>81</sup> Kr dating by <a href="#">Nagao and Miura (1993)</a> ; <sup>36</sup> Cl dating by <a href="#">Nishiizumi et al. (1992)</a> ; collected from eastern side of Nansen A
JARE-29 (Nansen B)	A 881069	0.03	H3.7	Nansen B (exact retrieval location unknown)		20 ± 1.4 ( <sup>14</sup> C)	<sup>14</sup> C dating at Arizona AMS Lab ( <a href="#">Ninagawa et al., 2006</a> )
	A 880793	0.07	H3.6			24.4 ± 1.5 ( <sup>14</sup> C)	<sup>14</sup> C dating at Arizona AMS Lab ( <a href="#">Ninagawa et al., 2006</a> )
	A 880676	0.11	H3.6			9.7 ± 1.3 ( <sup>14</sup> C)	<sup>14</sup> C dating at Arizona AMS Lab ( <a href="#">Ninagawa et al., 2006</a> )
	A 880620	0.10	H3.7			9.9 ± 1.3 ( <sup>14</sup> C)	<sup>14</sup> C dating at Arizona AMS Lab ( <a href="#">Ninagawa et al., 2006</a> )
	A 881216	0.12	H3.7			18.0 ± 1.3 ( <sup>14</sup> C)	<sup>14</sup> C dating at Arizona AMS Lab ( <a href="#">Ninagawa et al., 2006</a> )
	A 880624	0.09	H3.8			9.9 ± 1.3 ( <sup>14</sup> C)	<sup>14</sup> C dating at Arizona AMS Lab ( <a href="#">Ninagawa et al., 2006</a> )
	A 880684	0.06	H3.9			12.4 ± 1.3 ( <sup>14</sup> C)	<sup>14</sup> C dating at Arizona AMS Lab ( <a href="#">Ninagawa et al., 2006</a> )
	A 880863	0.02	H3.7			14.8 ± 1.3 ( <sup>14</sup> C)	<sup>14</sup> C dating at Arizona AMS Lab ( <a href="#">Ninagawa et al., 2006</a> )
JARE-54 BELARE	A 12084	1.51	H4	23.92056	−72.85741	10.7 ± 2.2 ( <sup>14</sup> C)	<sup>14</sup> C dating at Arizona AMS Lab
2012–2013 (Nansen B)	A 12105	1.13	H4	24.11539	−72.86960	37.8 ± 2.6 ( <sup>14</sup> C)	<sup>14</sup> C dating at Arizona AMS Lab
	A 12127	2.51	LL	24.29333	−72.92125	<51 ( <sup>36</sup> Cl)	<sup>36</sup> Cl dating at the ASTER AMS national facility at CEREGE
	A 12216	1.04	H6	24.34909	−72.86281	129 ± 28 ( <sup>36</sup> Cl)	<sup>36</sup> Cl dating at the ASTER AMS national facility at CEREGE
	A 12324	2.17	L4	24.23070	−72.88072	>43 ( <sup>14</sup> C)	<sup>14</sup> C dating at Arizona AMS Lab
	A 12326	6.42	L4	24.34971	−72.91552	49 ± 30 ( <sup>36</sup> Cl) >46 ( <sup>14</sup> C)	<sup>36</sup> Cl dating at the ASTER AMS national facility at CEREGE <sup>14</sup> C dating at Arizona AMS Lab
JARE-54 BELARE	A 12389	18.07	LL3-6	24.85403	−72.66674	65 ± 30 ( <sup>36</sup> Cl)	<sup>36</sup> Cl dating at the ASTER AMS national facility at CEREGE
2012–2013 (Nansen C)	A 12430	4.00	LL4	24.84283	−72.65079	15.8 ± 2.4 ( <sup>14</sup> C) <2.4 ( <sup>14</sup> C)	<sup>14</sup> C dating at Arizona AMS Lab <sup>14</sup> C dating at Arizona AMS Lab

age of the ice at the meteorite collection site (Folco et al., 2006) (see Appendix B for elaborate explanation). A common way to determine the terrestrial age of meteorites is through radiocarbon ( $^{14}\text{C}$ ) dating (Jull, 2006; Herzog et al., 2015). Given the short half-life time of  $^{14}\text{C}$  (5730 years), the method can generally only be applied to meteorites with a terrestrial age up to 40 ka (Jull, 2006), depending on the  $^{14}\text{C}$  blank correction. Eight meteorites from the ASUKA-88/JARE-29 expeditions on Nansen B were dated this way (Ninagawa et al., 2006) and found to have terrestrial ages between 9.7 and 24.4 ka old (Table 1; measurements at Arizona AMS Facility; see Appendix B for details). Unfortunately, these meteorite ages are of limited use to constrain the age of the ice, as the retrieval location of the meteorites is unknown. Furthermore, these eight meteorites weigh only between 19.3 and 119.3 g (Table 1), which is below the meteorite wind transport threshold of approximately 200 g (Folco et al., 2002). These meteorites may therefore have been transported by the strong katabatic winds (between t3 and t4 on Fig. 1a) and are as such potentially not representative for their collection location.

Meteorites collected during the JARE-54 – BELARE 2012–2013 expedition (Imae et al., 2015), for which the retrieval positions are precisely known (GPS coordinates with meter scale precision), were therefore selected for terrestrial age dating. Given the occurrence of strong year-round katabatic winds (Thierry et al., 2012; Imae et al., 2015), an initial selection of six meteorites weighing more than 1 kg was made (see also Appendix E). Four of these meteorites are well-spread across Nansen B (Fig. 5b), while the two other are from Nansen C. The terrestrial ages were determined through radiocarbon dating and ranged between a recent fall (<2.4 ka) and >45 ka (measurements at Arizona AMS Facility, United States of America; see Table 1 and Appendix B). Subsequently, the two meteorites with the oldest terrestrial ages (A 12324 and A 12326) were re-dated using the  $^{36}\text{Cl}$  method, together with two additional meteorites that were not radiocarbon dated (A 12127 and A 12216, measurements at ASTER AMS national facility at CEREGE, France; see Table 1 and Appendix B). Given the longer half-life time of  $^{36}\text{Cl}$  (301 ka), meteorites with older terrestrial ages can be dated (up to about 2 Ma), although the method is characterized by a larger uncertainty (Nishiizumi et al., 1989; Jull, 2006; Herzog et al., 2015). The  $^{36}\text{Cl}$  terrestrial age measurements resulted in ages between <51 and  $129 \pm 28$  ka (see Table 1).

## 5. REGIONAL ICE FLOW

Today, 3-D ice flow models constitute the most comprehensive method to determine the flow of an ice body (e.g. Huybrechts et al., 2007; Goelzer et al., 2012; Pattyn et al., 2017; Zekollari et al., 2017b). However, the use of a 3-D ice flow model is not justified here, as various boundary conditions have large uncertainties. The best estimates on the regional ice thickness are from the BEDMAP2 dataset (Fretwell et al., 2013), and recently performed airborne radar measurements of ice thickness over parts of the ice field and its surroundings (Eagles et al., 2018). These datasets suggest that the local ice thickness is typically in the

order of 1000 m around the ice field (see e.g. Fig. 4), but their low resolution (5 km for BEDMAP2, 10 km between flight lines for Eagles et al. (2018)) do not justify a setup with a detailed ice flow model over this region. Also, other boundary conditions, such as the surface mass balance (SMB) and the englacial ice temperatures, which determine the stiffness and thereby the velocity of the ice, remain relatively poorly constrained and therefore hamper the use of a 3-D ice flow model.

Therefore, to obtain an insight in the regional ice flow, satellite derived surface velocities are utilized. We rely on a recently released surface velocity dataset by Mouginot et al. (2017) and Rignot et al. (2017), in which measurements from a variety of sources (ALOS, COSMO-SKYMED, ERS-1, RADARSAT-1, RADARSAT-2 and SENTINEL-1A) are combined to derive the mean surface velocity over the Antarctic Ice Sheet for the period 1996–2016 at a 450 m spatial resolution (Fig. 3). Combining different sources results in errors on the horizontal surface velocity components that are generally lower compared to earlier versions of the dataset (Rignot et al., 2011) and products relying on a single platform (Callens et al., 2014; Fahnestock et al., 2016; Gardner et al., 2018). Despite this increased accuracy, for areas with low surface velocities, such as the Nansen ice field (Fig. 3), the errors on the velocities ( $1.4\text{--}2.3\text{ m a}^{-1}$  in Nansen B and C) remain of the same order of magnitude as the velocities (typically  $0.5\text{--}2.0\text{ m a}^{-1}$  for Nansen B,  $0.5\text{--}3.0\text{ m a}^{-1}$  for Nansen C; but can locally be only a few  $\text{cm a}^{-1}$ ). Consequently, in certain regions unrealistic ice flow is obtained, such as an upstream ice flow over large spatial scales. To correct for this unrealistic ice flow, the direction of the satellite derived surface velocity vectors (Mouginot et al., 2017; Rignot et al., 2017) is adapted by making use of the surface topography data. The surface velocity vectors are forced to follow the steepest negative surface gradient (as derived from the BEDMAP2 dataset; Fretwell et al., 2013) within the error bars for both the x- and y-direction (Fig. 6). At each location, the surface gradient is determined over a distance of several kilometres, corresponding to several times the local ice thickness. This is used to mimic the effect of longitudinal stress gradients, causing the ice flow to depend on the surrounding topography, and not only the local geometry (Kamb and Echelmayer, 1986; Callens et al., 2014). The order of magnitude of the satellite derived surface velocities ( $0.5\text{--}3.0\text{ m a}^{-1}$ ) is confirmed by ice flow modelling, utilizing typical ice thicknesses and englacial ice temperatures that can be expected for the Nansen ice field (details in Appendix C).

## 6. DISCUSSION

### 6.1. Dating and distribution of surface ice

The  $\delta^{18}\text{O}$  signal observed in the surface samples on Nansen B and the occurrence of three pronounced clusters (Fig. 5a), suggest that ice from both glacial and interglacial periods is present at the surface. The difference in  $\delta^{18}\text{O}$  between the ‘low  $\delta^{18}\text{O}$  areas’ (Nansen B1 and Nansen B3) and the ‘high  $\delta^{18}\text{O}$  area’ (Nansen B2) is around 5–7‰,



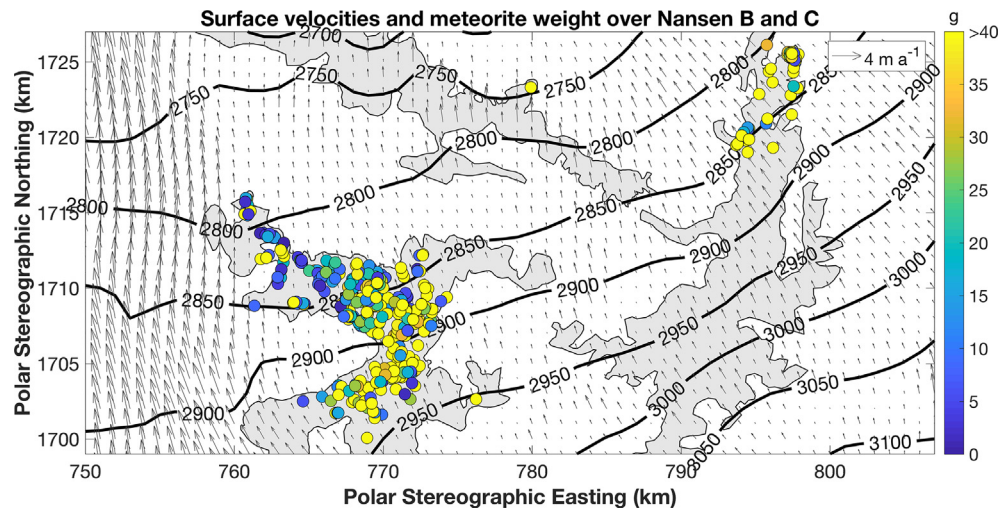


Fig. 6. (a) Surface ice flow over Nansen B and C ice fields, based on a hybrid method in which satellite derived surface velocity direction (Mouginot et al., 2017; Rignot et al., 2017) is corrected based on surface topography (Fretwell et al., 2013) (see text for details). Arrows are proportional to the surface velocity magnitude. The thick black lines represent surface elevation contours (Fretwell et al., 2013), while the coloured dots represent the mass of the meteorites collected in 2012–2013. The shaded areas correspond to the blue ice fields. (For interpretation of the references to colour in this figure legend, the reader is referred to the web version of this article.)

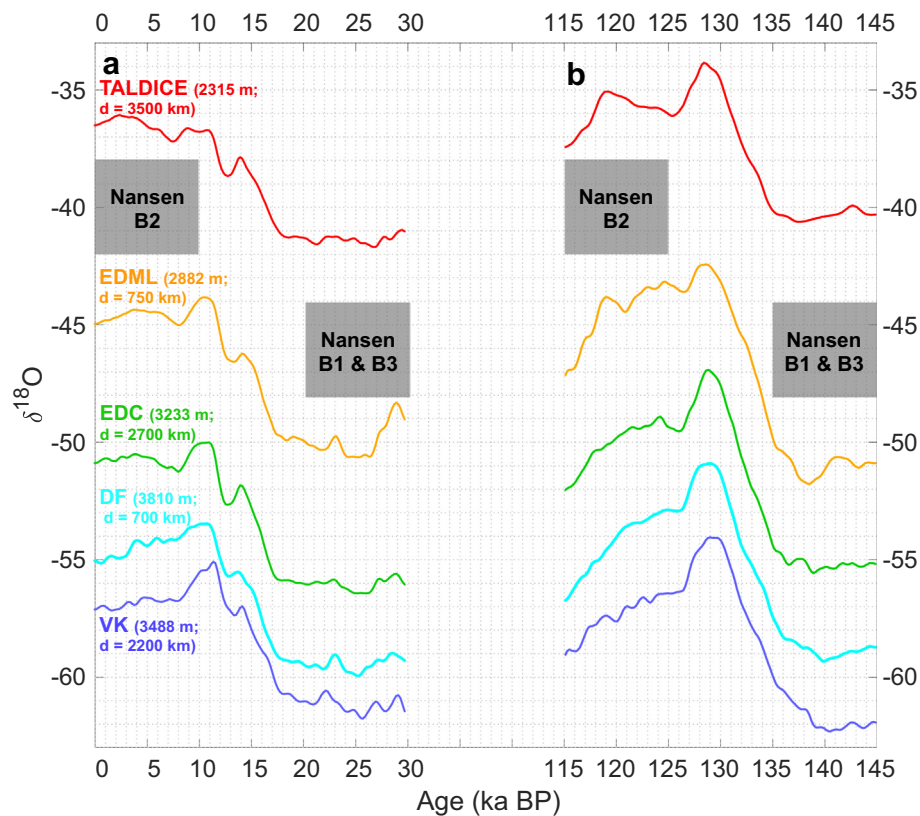


Fig. 7.  $\delta^{18}\text{O}$  variations (in ‰, original records) measured from selected major ice core drillings (TALDICE = Talos Dome; EDML = EPICA Dronning Maud Land; EDC = EPICA Dome C; DF = Dome Fuji; VK = Vostok), displayed on the EDC3 age scale (in ka), together with measured  $\delta^{18}\text{O}$  ranges for Nansen B1 and B3 (−48‰ to −44‰) and Nansen B2 (−42‰ to −38‰) for (a) the current interglacial-glacial transition and (b) the previous interglacial-glacial transition.  $\delta^{18}\text{O}$  data from Masson-Delmotte et al. (2011). For every major ice core, the two related numbers correspond to the surface elevation and the distance to the Nansen ice field.



which corresponds exactly to the offset observed between glacial and interglacial periods in Antarctic deep drilling cores (e.g. [Masson-Delmotte et al., 2011](#)). However, solely relying on the  $\delta^{18}\text{O}$  values does not allow determining from which (inter)glacial period the surface ice originates, as the clusters fit various glacial-interglacial transitions, as illustrated for the current and previous interglacial-glacial transition in [Fig. 7](#) (discussed further in [Section 6.5](#)).

#### 6.1.1. Nansen B

As the terrestrial age of the meteorites are interpreted to reflect minimum age estimates for the underlying ice (see [Appendix B](#) and e.g. [Folco et al., 2006](#)), combining those ages with the  $\delta^{18}\text{O}$  measurements indicates that the ice on Nansen B formed during the last glacial period (Nansen B1 and Nansen B3) and during the Last Interglacial (LIG, ca. 130–115 ka ago) (Nansen B2). The differences in terrestrial ages between meteorites collected in each other's vicinity is explained by a different timing of appearance at the surface. In the case of Nansen B2, it is probable that meteorite A12216 ( $129 \pm 28$  ka) appeared recently at the surface, while meteorite A12324 ( $49 \pm 30$  ka) has likely appeared higher upstream. As a consequence, meteorite A12324 may have travelled over a longer distance, increasing the difference between the terrestrial age and the age of the underlying ice (see e.g. [Folco et al., 2006](#)).

In combination with the corrected surface velocities, this suggests that Nansen B1 and B2 are stratigraphically connected, with Nansen B2 being the prolongation of Nansen B1 (Nansen B1 is upstream from Nansen B2 in the schematic representation in [Fig. 1a](#)). Although the area south of Nansen B1 was not visited, the sequence of isotopic clusters and the regional ice flow imply that here, ice from the present-day interglacial and the end of the previous glacial period is present.

For Nansen B3, the distribution of ice is possibly more complex, as two potential supply mechanisms are identified:

- (i) A fraction of the meteorites/ice on Nansen B3 may originate from a (relatively small) separate source area, which is independent from that of Nansen B1 and B2. This is supported by the observation that the southernmost ice samples collected on Nansen B3 show higher  $\delta^{18}\text{O}$  values (see [Fig. 5](#)), which may suggest that this ice is from the present interglacial. The relatively young terrestrial ages ( $<40$  ka) for the meteorites recovered on Nansen B3 ([Fig. 5b](#)) also support this mechanism.
- (ii) Another supply mechanism may consist of meteorites that exited Nansen B1 through ice flow (cf. t4 on [Fig. 1a](#)), re-entered the ice sheet (at shallow depth) below the snowfield between Nansen B1 and B3 (t5 on [Fig. 1a](#)), and subsequently reappeared at the surface of Nansen B3 (follow trajectory on [Fig. 1a](#) after t5 and forced back to the surface on Nansen B3). Such mechanism could also explain that the collected meteorites/ice on Nansen B3 are younger than those found on Nansen B2.

#### 6.1.2. Nansen C

For the northern part of Nansen C, the high  $\delta^{18}\text{O}$  values ( $-42$  to  $-36\text{‰}$ ), combined with the young terrestrial age of meteorites, suggest that the ice is younger than the Last Glacial Maximum (LGM). Here, additional constraints on the age of the ice can be derived from volcanic ashes that were extracted from local tephra-bearing ice samples during the 2012–2013 expedition (see [Fig. 5a](#) for location). By comparing the chemical composition of this volcanic ash with that of other ashes retrieved from major Antarctic ice cores, [Oda et al. \(2016\)](#) proposed that the volcanic ashes in the northern part of Nansen C originate from the South Sandwich Islands (for details on geochemical composition ash layers, refer to Table 3 in [Oda et al. \(2016\)](#)). The chemical composition of the ashes correlates particularly well with that of ashes from two post-LGM eruptions (see Table 4 in [Oda et al. \(2016\)](#)):

- (i) at about 10.7 ka BP. These ashes are found at 340 m depth in EPICA-Dome C ([Narcisi et al., 2005](#)).
- (ii) at about 3.5 ka BP. These ashes are found at 133 m depth in EPICA-Dome C ([Narcisi et al., 2005](#)) and at 100 m depth in Vostok ([Palais et al., 1989](#); [Basile et al., 2001](#)).

It is thus likely that the ashes retrieved on Nansen C correspond to one of these two major late/post-LGM events. Although the chemical composition of some older ash layers from Antarctic ice cores also correlates relatively well with that of the Nansen C ash layer (e.g. ash layer at 505 m depth in Dome Fuji, dated at ca. 20 ka BP ([Kohno et al., 2004](#); [Fujita et al., 2015](#))), these are all from previous glacial periods, in disagreement with the high  $\delta^{18}\text{O}$  values for the ice at the surface of Nansen C. For the LIG, when  $\delta^{18}\text{O}$  values were also high (cf. [Fig. 7b](#)), the chemical composition of the ashes retrieved from major ice cores does not resemble that of the ash layer retrieved at the surface on Nansen C. The compositional analysis of the ashes, combined with the isotopic signatures of the surface samples and the terrestrial ages of the meteorites, strongly suggest that the surface ice on Nansen C originates from after the LGM.

#### 6.1.3. Nansen A

Nansen A was not visited during the 2012–2013 field campaign. Isotopic analyses of surface blue ice samples and terrestrial dating of meteorites can therefore not be used to constrain the age of the local ice. Most likely the distribution of meteorites (and surface ice) is relatively complex here because most meteorites that exit Nansen B and Nansen C (cf. t4 on [Fig. 1a](#)), re-enter the ice sheet (at shallow depth, t5) and subsequently reappear at the surface in Nansen A (cf. the potential mechanism (ii) described for Nansen B3) (see [Fig. 6](#)). Therefore, both relatively young (from Nansen C) and older (from Nansen B) ice and meteorites are anticipated to mix at Nansen A.

## 6.2. Meteorite mass, weathering, pairing and surface residence time

### 6.2.1. Meteorite mass and weathering

A clear spatial pattern in the mass of the collected meteorites (fragments) is observed (Fig. 6). On Nansen B1, Nansen B2 and Nansen C, meteorites show little to no weathering, and here meteorites of all sizes are collected, with many (47%) weighing more than 40 g (Fig. 4b). However, for Nansen B3 the meteorites are small, mostly weighing less than 40 g (in 85% of cases), and field observations suggest (Imae et al., 2015) that these have been subjected to more substantial weathering in general (vs. Nansen B1 and B2). As weathering mainly occurs at the surface (e.g. Koeberl and Cassidy, 1991; Scherer et al., 1997; Welten et al., 1997, 2008; Pourkhorsandi et al., 2017), this likely indicates that a substantial fraction of the meteorites on Nansen B3 has been transported at the surface for prolonged periods of time. This may result from particularly low surface velocities at Nansen B3 (which are lower than over Nansen B1 and B2, cf. Fig. 6). However, it could also support the earlier proposed mechanism in which most meteorites on Nansen B3 were previously transported at the surface of Nansen B1, after which they re-entered the ice sheet and subsequently re-appeared at the surface. Furthermore, the preferential transport of light meteorites by wind may also play a role here, and a part of these meteorites may have been transported from Nansen B2 to Nansen B3 (cf. Zwinger et al., 2015). The meteorites on Nansen B2 are on average slightly smaller (40% of meteorites weighing more than 40 g) and slightly more weathered in general (Imae et al., 2015) than those on Nansen B1 (60% of meteorites weighing more than 40 g) (Fig. 6), which may be explained as the effect of a long travel time at the surface for some of these, i.e. if they first appeared at the surface on the southern part of Nansen B1. These are complemented by ‘fresh meteorites’, which appear at the surface of Nansen B2 for the first time, explaining also why many large meteorites, with limited weathering, are found here.

The meteorites collected during the JARE-54/BELARE 2012–2013 expedition were on average much heavier (ca. 175 g average mass) and less weathered than those collected during the BELARE 2010–2011 mission on Nansen A (ca. 30 g average mass) (Goderis et al., 2011; Imae et al., 2015). Ninagawa et al. (2005) also reported older terrestrial ages (based on thermoluminescence studies) and higher degree of weathering for meteorites on Nansen A compared to those on Nansen B. This supports the proposed mechanism, in which most of the meteorites collected on Nansen A are meteorites that indeed reached the surface on Nansen B and C, where they were transported at the surface (i.e. undergoing weathering), before re-entering the ice sheet (at shallow depth) to reappear on Nansen A.

### 6.2.2. Meteorite falls and pairing

Some of the meteorites collected on the Nansen ice field may be fragments from an individual fall, as a fragmentation of meteorites may occur during (i) atmospheric passage and/or (ii) during their terrestrial history (Benoit et al., 2000). For Antarctic meteorites the number of meteorite

fragments per fall is typically in the range of 2 to 6, i.e. with a pairing ratio varying between 1:2 and 1:6 (Lindstrom and Score, 1995; Benoit et al., 2000). Given the relatively limited weathering of meteorites on the Nansen ice field compared to other Antarctic sites at lower elevation (where higher temperatures and potential presence of meltwater favour weathering), the pairing is expected to be at the lower end of this range. This is confirmed by a previous pairing study on Nansen meteorites by Ikeda and Kimura (1992), who found that the ordinary chondrites (which make up 86% of all meteorites, by number; Meteoritical Bulletin Database, 2018) make up for less than two fragments per fall. An assessment of the mass distribution of the collected meteorites when compared to a mass-dependent function for meteorite falls (Halliday et al., 1989) also supports a relatively low pairing: e.g. from this relationship, without fragmentation, the ratio between meteorites weighing more than 10 g and those weighing more than 100 g should be around 3:1, while in the collected Nansen meteorites this is about 4:1. These elements suggest that the fragments per fall at the surface of Nansen are at the lower end of the values found in the literature, and we estimate this number to range from 2 to 4.

### 6.2.3. Meteorite mean surface residence time

Many of the meteorites collected on the Nansen ice field may have been exposed at the surface since a long time. Here, we describe this process through the meteorite's mean surface residence time (MSRT), which is used further on to assess the characteristics of the Nansen blue ice field (e.g. infall rate, supply rate of fresh meteorites, estimation of source area size). The MSRT is a similar concept to the ‘surface exposure age’ introduced by Benoit (1995) based on natural thermoluminescence (TL), and the ‘on-ice travel time’ described by Folco et al. (2006). It corresponds to the average time between the appearance of a meteorite at the surface of an ice field ( $t_4$  on Fig. 1a) and its disappearance from this particular ice field (as it flows out of the field, at  $t_5$ ). Here, we derive the MSRT from the corrected surface velocities (Section 5; Fig. 6); two distinct approaches are considered:

- The MSRT is obtained by assuming a spatially evenly distributed appearance rate of meteorites at the ice field surface and by subsequently forcing the meteorites to move at the surface, along with the ice flow, until they exit the ice field.
- Starting from their retrieval location, the meteorites are projected at the surface both forward and backward (i.e. following the opposite direction of the ice flow) with time, until they exit the ice field at both ends. Here, the surface residence time of each meteorite corresponds to half the time it remains on the ice field (i.e. half the time needed for the hypothetical transport from the upper to the lower ice field boundary).

Through the application of these two approaches, MSRTs of 5600 years (approach *a*) and 5900 years (approach *b*) are obtained for Nansen B. As the ice flow

and the katabatic winds are largely in the same direction (Imae et al., 2015), the MSRT may be reduced, as light meteorites (<200 g) are prone to transport by wind. Accounting for this effect and considering the uncertainties and possible changes in the surface velocity field over time, the MSRT on Nansen B is estimated to be between 4000 and 6000 years. Applying the same principles to the northern part of Nansen C leads to a MSRT time of 3300 years (approach *a*) and 3000 years (approach *b*), respectively. Considering the effect of the katabatic winds and uncertainties associated with the surface velocity field, it is estimated that the MSRT for meteorites on the northern part of Nansen C is between 2500 and 3500 years.

### 6.3. Source area size, location and supply mechanism

#### 6.3.1. Source area size

In a stable glacial system, consisting of an accumulation area and an ablation area, the integrated surface mass balance (SMB) is zero. For the Nansen meteorite trap, by estimating the surface mass balance in the ablation area (i.e. the Nansen ice field) and the accumulation area (i.e. the source area of the Nansen ice field), the ratio between these areas can be determined.

Based on simulations with an energy-balance model, which is forced with automatic weather station (AWS) data and a blue ice albedo of 0.57 (Lenaerts et al., 2017), the annual surface mass balance over the Nansen ice field is estimated to be between  $-125$  and  $-75$  mm w.e.  $a^{-1}$  (all details are provided in Appendix D). For the accumulation area, the SMB is derived from a high-resolution (5.5 km) simulation with the RACMO2 regional climate model and estimated to be between 20 and 50 mm water equivalent per year (mm w.e.  $a^{-1}$ ; refer to Appendix D for details). These surface mass balance estimates thus suggest that the ratio between the source area and the Nansen ice field varies between 75:50 (1.5:1) and 125:20 (6.25:1). With a visited area of about 100 km<sup>2</sup> for Nansen B; the source area is thus estimated to be between 150 and 625 km<sup>2</sup>.

#### 6.3.2. Source area location and supply mechanism

As the estimation of the source area size varies by a factor of four and the regional topography may have changed over time, it is difficult to address the exact location of the source area. However, a rough estimate of the source area location can be obtained by projecting the meteorites back in time. For this, we assume that the surface velocities are constant in time and that the meteorites within the ice sheet are transported at the same velocity as at the surface. As sliding acts at the base and most deformation occurs in the lowest part of the ice sheet (e.g. Huybrechts et al., 2011; Pattyn et al., 2017; Hindmarsh, 2018), this is a reasonable assumption. For more realistic insights into the transport of meteorites within the ice sheet, a 3-D ice flow model would be needed in which the particles can be tracked back in time (e.g. Huybrechts et al., 2007), but as argued before, given the large uncertainties in boundary conditions, this is not justified here. The duration of the projection is determined by the oldest terrestrial age of a meteorite (i.e. estimation of the oldest age of the ice

retrieved), which is approximately 140 ka for Nansen B and about 20 ka for the northern part of Nansen C. Following this method, the source area of Nansen B could reach as far as 150 km to the south and reach up to 3350 m a.s.l. (palaeoclimatic conditions of the source region are addressed in Section 6.5). This indicates that the source area is located south of the ice field and that it likely has a rather elongated form (i.e. a large north-south to east-west ratio). It should be noted that some meteorites that reached the ice sheet surface further south likely also cross the Nansen ice field through their englacial trajectory. However, given the long trajectory towards the Nansen ice field, these meteorites reach deeper parts of the ice sheet and are therefore thought to be underneath the surface on the Nansen blue ice field (cf. lowest flow lines in Fig. 1a).

For Nansen C, the surface velocities indicate that the source area is likely located to the east of the ice field. Here, the source area is constrained by a surface ridge (Fig. 3), which explains the lack of glacial ice at the surface of Nansen C. For the central and southern parts of Nansen C, which were not revisited since the 1980s, the source area is presumably situated more to the south, but it is most likely also confined by the ridge situated east of the ice field.

Combining the available information on surface and subglacial topography with the estimated source areas thus suggests that the Sør Rondane Mountains do not directly act as the natural barrier causing the meteorites to reach the surface. The Nansen ice field is not a so-called ‘closed type’ blue ice area, but should be interpreted as an ‘open type’ blue ice area, in which the ice flow is potentially slowed down by subglacial bedrock ridges and forced upwards in combination with surface ablation (Grinsted et al., 2003; Sinisalo and Moore, 2010). For Nansen B, the ‘open’ character of the blue ice area explains the limitation in the age of the ice (until the previous interglacial), as the oldest ice and meteorites are thought not to reach the surface on the ice field (Grinsted et al., 2003 cf. lowest flow lines in Fig. 1a).

### 6.4. Implications for infall rate, direct fall and supply rate

#### 6.4.1. Infall rate

The infall rate of meteorites is defined as the number of meteorites entering the atmosphere above a certain weight threshold for a certain area and per time unit. In the literature, infall rates are typically estimated based on recovery statistics and weathering rates from arid areas, and vary broadly by a factor of three, from 36 to 116 meteorites ( $>10$  g)/ $10^6$  km<sup>2</sup>/a (Bland, 2001). Another widely used estimate is the 83 meteorites ( $>10$  g)/ $10^6$  km<sup>2</sup>/a derived by Halliday et al. (1989) based on meteoroid observations. Recovery statistics from Antarctic meteorites form an interesting alternative to derive infall rates, but their use is generally hampered by various uncertainties (Zolensky et al., 2006). However, for the Nansen ice field the large and diverse set of collected data can be used to provide insights into the infall rate by relying on an alternative estimate of the source area (vs. the estimate based on SMB; see Section 6.3.1.).

The source area ( $A$ , in km<sup>2</sup>), can be related to the mean surface residence time (MSRT) of a meteorite at the surface



( $T_{res}$ , in a), the number of (pairing-corrected) meteorites ( $M$ , dimensionless), and the meteorite infall rate ( $I$ ):

$$A = M / (I * T_{res}) \quad (1)$$

Given that the supply of meteorites to the ice field ( $S$ , in meteorites  $a^{-1}$ ) corresponds to:

$$S = M / T_{res} \quad (2)$$

Eq. (1) can be rewritten as:

$$A = S / I \quad (3)$$

For Nansen B, a plausible range of values for the supply of meteorites to the ice field ( $S$ ) can be obtained by combining a lower and upper boundary estimate of (i)  $T_{res}$  (between 4 and 6 ka for Nansen B, see Section 6.2.3) and (ii)  $M$ , which is estimated to be in the range between:

- 325 pairing-corrected meteorites: this estimate assumes that almost the entirety of meteorites on Nansen B was found (1300 meteorites), and that the pairing is at the higher end of the range (1:4). Given the mass distribution in the meteorites found on Nansen B (Fig. 4a and b), a total of 325 pairing-corrected meteorites translates into about 270 pairing-corrected meteorites with a weight of 10 g or more.
- 750 pairing-corrected meteorites: this approximation assumes that not all meteorites were found yet (1500 meteorites) and that the pairing is at the lower end of the range (1:2). This results in about 625 pairing-corrected meteorites weighing 10 g or more.

The supply of meteorites ( $>10$  g) to Nansen B is thus somewhere between  $270/6000 = 0.045$  meteorites  $a^{-1}$  and  $625/4000 = 0.156$  meteorites  $a^{-1}$  (Eq. (2)). This estimate for  $S$ , combined with the range of plausible values for  $I$  from the literature, allows us to calculate the source area

size ( $A$ ) based on Eq. (3) (Fig. 8). A realistic ratio between the accumulation and the ablation area size as determined from SMB modelling (i.e. between 1.5:1 and 6.25:1, see Section 6.3.1 and Appendix D) can only be obtained for a relatively large accumulation area (ratio of accumulation to ablation area above 3:1) with a supply ratio lower than  $<0.1$  pairing-corrected meteorites ( $>10$  g  $a^{-1}$ ), combined with an infall rate above 60 meteorites ( $>10$  g)/ $10^6$  km<sup>2</sup>/a (Fig. 8a). Similar results are obtained for the northern part of Nansen C ( $M = 33$ –104 pairing-corrected meteorites  $>10$  g), where based on Eq. (3) the entire range of infall rates from the literature is realistic, but where higher values for  $I$  are deemed to be more likely (Fig. 8b). Besides the implications for the infall rate, the low supply ratio may indicate that the number of meteorites is relatively low, i.e. most meteorites were found and a substantial fraction of them represents fragments of a more limited number of falls, and/or that the MSRT of meteorites is at the higher end of the estimated range.

#### 6.4.2. Supply rate

Applying a MSRT of 4 ka to Nansen B and assuming there are 1500 meteorites at the surface of this ice field, an upper estimated supply rate of 0.4 meteorites  $a^{-1}$  is obtained. Taking into account the infall rates from the literature and the source area size estimates, Eq. (3) and Fig. 8 even suggest that the upper boundary is lower than this. During the 25-year period between the JARE-29 and JARE-54/BELARE 2012–2013 expeditions, less than 10 new meteorites thus reached the surface of Nansen B. From this, we can conclude that the retrieval of 368 meteorites during the JARE-54/BELARE 2012–2013 expedition on Nansen B is therefore not related to a supply of new ('fresh') meteorites, but rather indicates that many meteorites were not found during the previous expeditions. Some meteorites may have been found in sites that were

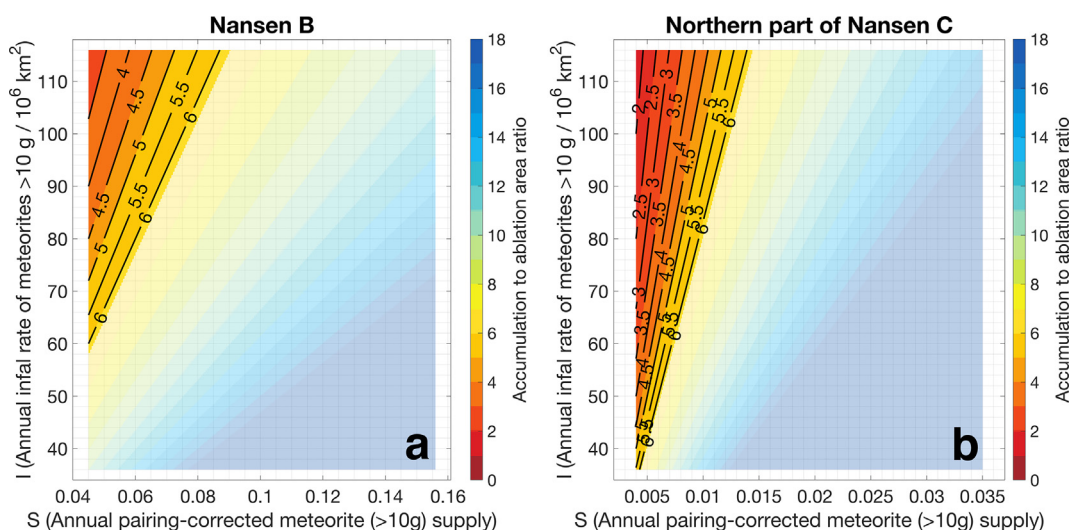


Fig. 8. Ratio between the accumulation and source area for the Nansen B ice field (panel a) and the northern part of the Nansen C ice field (panel b), as calculated from Eq. (3). The ratios that fall outside of the range determined from SMB modelling (1.5:1–6.25:1, see Section 6.3.1) are shown in transparent colours. (For interpretation of the references to colour in this figure legend, the reader is referred to the web version of this article.)

previously not visited on Nansen B, while other meteorites may have been overlooked during the JARE-29 expedition. Migrating snow patches and ice field boundaries may have exposed meteorites in the 2012–2013 field season that were snow-covered during the JARE-29 expedition.

#### 6.4.3. Direct fall

The role of direct falls (Huss, 1990), i.e. the fraction between the meteorites that fell on the surface of the ice field directly and those that reached the ice field through an englacial transport, can be determined from the ratio between the accumulation area and ablation area (assuming a spatially evenly distributed appearance of meteorites at the surface after englacial transport). Implementing an accumulation to ablation area ratio between 6.25:1 to 3:1 (see Section 6.4.1), this suggests that between 14% (1:7.25) and 25% (1:4) of the meteorites on the surface of the ice field are from direct fall.

An alternative and independent estimate for the role of direct fall can be obtained by estimating the number of meteorites that fall on the surface during the MSRT of meteorites on a particular ice field. When considering this approach, it should be noted that light meteorites may be transported by katabatic winds, but that the resulting effect on the total number of meteorites on the field is considered to be relatively limited. For Nansen B, where an area of about 100 km<sup>2</sup> was explored (see Figs. 4a and 5), assuming an upper limit for the infall rate of 116 falls over 10 g/10<sup>6</sup> km<sup>2</sup>/a (Bland, 2001) and a long MSRT of 6 ka, results in a total of 69.6 direct falls (>10 g). By relying on a lower limit for the infall rate of 36 falls over >10 g/10<sup>6</sup> km<sup>2</sup>/year (Bland, 2001) and a MSRT of 4 ka, a lower bound estimate of 14.4 direct falls (>10 g) is obtained. The relative contribution of direct infall relies on the total number of meteorites present at the surface of Nansen B before the meteorite recovery expeditions (see Section 6.4.1. for estimates). From this, the amount of meteorites on Nansen B deriving from direct falls can be estimated to be between 2.3% (14.4/625) and 25.8% (69.6/270). Given the assumed relatively high infall rate (see Section 6.4.1), the higher end of this range is more likely, which also agrees with the 14–25% estimate from the accumulation to ablation area ratio. Combining both estimates therefore suggests that about 15–25% of all collected meteorites fell on the Nansen ice field directly. It should be noted that this estimate is higher than suggested by the limited sample suite of twenty meteorites for which the terrestrial age was determined (Table 1). From these twenty meteorites, only one (A 12430) results from a direct fall, as its terrestrial age (<2.4 ka) is younger than the time needed to transport it from the snowfield to the collection site. One other meteorite (A12084) may represent a direct fall, which landed on Nansen B1, re-entered the ice sheet, and subsequently reappeared on Nansen B3 (cf. Section 6.1.1).

#### 6.5. Implications for palaeoclimate and palaeoglaciology

Given the absence of fixed age estimates and the presence of large uncertainties in boundary conditions, which inhibit the use of a complex ice flow model, it is not possible

to derive a continuous palaeoclimatic record from the surface blue ice samples collected on the Nansen ice field (e.g. Spaulding et al., 2013). The magnitude of the isotopic signal and the difference between isotopic clusters can however be used to shed a light on the palaeo-conditions that reigned over this region.

The  $\delta^{18}\text{O}$  values at Nansen B are consistently less negative than those measured at the EPICA Dronning Maud Land (EDML) drill site (see Fig. 7), which is located 750 km to the west, at about the same elevation (2800–2950 m a.s.l. for Nansen B vs. 2882 m a.s.l. for EDML). For both the EDML drill site and the Nansen B ice field, the elevation at the formation site is higher than the present-day elevation. For Nansen B, this elevation difference is estimated to be up to 350–400 m between the LIG formation location and present-day elevation (see Section 6.3.2), while for EDML the LIG ice was formed about 300 m higher (Huybrechts et al., 2007). The distance to the ocean differs for both sites, as the Nansen blue ice field is located about 300–400 km from the coast (depending on direction), while for the EDML drill the coast is 550–600 km away. This may explain a part of the difference in  $\delta^{18}\text{O}$  between both sites, as air masses preferentially precipitate heavy oxygen isotopes while advancing over the continent (e.g. Jouzel et al., 2003). The  $\delta^{18}\text{O}$  difference is however larger than would be expected from the preferential precipitation of heavy oxygen isotopes only. We therefore suggest that the  $\delta^{18}\text{O}$  difference between both sites may also reflect differences in surface temperatures. The constantly lower  $\delta^{18}\text{O}$  values for EDML suggest that temperatures at the time of formation were lower for EDML than for the Nansen ice field. The  $\delta^{18}\text{O}$  difference between both records varies from approximately 3–5‰ (see Fig. 7), which, after correcting for the difference in distance to the ocean for both sites (correction of about 1‰), agrees with a difference between 2 and 4‰. Assuming the Antarctic wide isotope-temperature relationship of 0.8 ‰/°C (Masson-Delmotte et al., 2008, Fig. 6b), this corresponds to a temperature difference of about 2.5–5 °C. It should be noted that this estimation is dependent on the isotope-temperature relationship, which is known to vary spatially and over time (Masson-Delmotte et al., 2008; Touzeau et al., 2016). However, Atmospheric General Circulation Models (AGCMs) suggest that the modern temperature-isotope relationship for central Antarctica is a good approximation for glacial to present-day changes (Jouzel et al., 2003). Note that the difference in  $\delta^{18}\text{O}$  (and thus temperature) will even be slightly more pronounced when considering that the formation site is likely higher for Nansen B compared to EDML. The  $\delta^{18}\text{O}$  difference should be interpreted with care, but in general, it indicates that it is now, and consistently was, warmer on the (accumulation area of the) Nansen ice field than at the (accumulation area of the) EDML drill site (Kohnen station) since the Last Interglacial.

The relative changes in surface elevation over time, which affect the  $\delta^{18}\text{O}$  signal, are believed to have been roughly similar for both sites, as the  $\delta^{18}\text{O}$  differences between both records remain largely the same over time. The local elevation at both sites may have evolved

in a similar way over time, but the similar signal more likely indicates that surface elevation changes at both sites have been relatively limited. This suggests the topography over Dronning Maud Land was relatively stable during the last glacial and the present interglacial, providing additional support for studies suggesting limited changes in elevation at Kohnen (up to ca. 100 m between glacial-interglacial cycles; Huybrechts et al., 2007) and around the Sør Rondane (evidence from morainic material and exposure dating; Mackintosh et al., 2014; Suganuma et al., 2014), in line with a stable interior East Antarctic ice sheet over this time period (e.g. Bentley et al., 2014; Mackintosh et al., 2014; Folco et al., 2016; Bader et al., 2017; Kaplan et al., 2017; Genge et al., 2018; Van Ginneken et al., 2018).

## 7. CONCLUSIONS

Combining different types of field, laboratory and remote sensing data allowed us to better constrain the meteorite concentration mechanism at the Nansen ice field. On Nansen B, one of the largest spatial patterns in contrasting oxygen isotopic values to date was found, indicating that ice from both glacial and interglacial periods is present at the surface. By combining this data with terrestrial ages of large meteorites, we suggest that this ice is from the previous glacial (ca. 115–15 ka BP) and interglacial period (ca. 130–115 ka BP). By using information from previously collected ash layers (Oda et al., 2016), the ice on the northern part of Nansen C was found to be from after the Last Glacial Maximum.

The size of the source areas of Nansen B and C was estimated based on the ratio between the modelled SMB in the ablation area (the ice field) and the accumulation area (the source area). The relatively limited source area size of a few hundred square kilometres suggests that the Sør Rondane Mountains do not act as a barrier (i.e. ‘closed type’ blue ice area), but rather that the meteorite trap acts on a smaller spatial scale and is therefore an ‘open type’ blue ice area.

In this study, we also used and further elaborated the concept of the mean surface residence time (MSRT) of a meteorite, which we derived from corrected state-of-the-art satellite-derived velocity data. We showed that the MSRT can be used, in combination with other field measurements, to get an insight into:

- (i) The infall rate of meteorites. Our analyses do not allow making a detailed statement on the debated infall rate of meteorites, but suggest that the values at the lower end of the literature are not compatible with the various datasets and quantities (including the MSRT), therefore suggesting that the infall rate is at the higher end of the range found in the literature.
- (ii) The role of direct infall. It was estimated that between 15 and 25% of all collected meteorites (>10 g) directly fell on the ice field, indicating that the importance of direct infall may be relatively large and not negligible.
- (iii) The supply rate of new meteorites. For Nansen B, it was estimated that less than 0.4 new meteorites reach the surface every year. This implies that meteorites found during the 2012/2013 expedition are mainly those that were not found during expeditions conducted 25 years earlier, rather than a recent resupply. By now, it is likely that most of the meteorites on Nansen A, B and the northern part of Nansen C have been found. Additional meteorites may still be collected in the future, in part due to the migration of the ice field boundary and local snow patches, but given the limited supply of fresh meteorites, the numbers are expected to be substantially lower than for the 2012/2013 expedition. Future meteorite search expeditions on this ice field should focus on new, not well-explored regions, such as the southern part of Nansen B (which is difficult to access with snowmobiles) and the southern part of Nansen C (which was only visited once), rather than a revisit of Nansen A or B.

In summary, the interdisciplinary approach employed in this study leads to a better understanding of the mechanism behind the Nansen meteorite trap. Some variables and parameters used in this study have still a significant uncertainty, and it is likely that future measurements and observations (e.g. of ice flow, SMB, meteorite weathering and fragmentation) will allow to further constrain the mechanisms behind this ice trap. Some of the findings are specific to the Nansen meteorite trap, but the developed methodology and the use of the mean surface residence time (MSRT) concept based on satellite derived surface velocities have the potential to improve our understanding of other Antarctic meteorite traps. As such, this methodology could also be used to plan future expeditions and may be applied to identify new meteorite collection sites (e.g. by identifying blue ice areas with long MSRTs).

Finally, the oxygen isotopic signal of the surface blue ice samples could not be used to identify continuous stratigraphic series, but the absolute difference between the clusters allowed for certain interpretations about past climatic and environmental conditions. These suggest that temperatures over the Nansen ice field were likely warmer than at the Kohnen station (EDML drill site) since the Last Interglacial. Furthermore, the relatively constant difference between the two records suggests that, regionally, the topography did not change since the Last Interglacial. In future works, more palaeoclimatic information could be obtained by dating the surface blue ice samples directly (e.g. through isotopic analyses of gases). This will be crucial in the ‘quest for the oldest ice’ and allow to re-collect older ice than that from deep drilling projects.

## ACKNOWLEDGEMENTS

We thank everyone who participated in the JARE-54 & BELARE 2012/2013 joint expedition, and especially Naoya Imae who led the Japanese team. BELARE 2012/2013 was funded



through the Belgian Science Policy Office (BELSPO) projects SAMBA and BELAM. HZ thanks Sophie Berger for helping with the retrieval of surface velocity data and Kevin De Bondt for introducing him to the Picarro Cavity Ring-Down Spectrometer. We thank Paul Smeets and Carleen Reijmer (IMAU, Utrecht University) for providing AWS observations. HZ was funded through a fellowship of the Research Foundation Flanders (FWO) (grant 11T0114N/11T0116N) and performed a substantial part of this research at ETH Zürich and WSL Birmensdorf, thanks to an FWO travel grant for a long stay abroad (V427216N), and a WSL innovative project grant. VD thanks the FRS-FNRS and ERC StG “ISoSyC” for present funding. PC and SG acknowledge the support of the VUB Strategic Research Program. JG acknowledges funding from the French Agence Nationale de la Recherche (grant ANR-13-BS05-0009). We are grateful for the very thorough and thoughtful comments by two anonymous reviewers, which greatly helped us to improve the manuscript.

## APPENDIX A. SURFACE BLUE ICE SAMPLES COLLECTION AND ANALYSES

All blue ice surface samples were collected during the 2012–2013 meteorite recovery operations. When a meteorite was found by an expedition member, and when time and meteorological conditions allowed sampling, a surface blue ice sample was collected by another expedition member. The distance between the meteorite collection site and surface blue ice collection site varied between a few metres up to about 100 m, depending on the search party formation and the respective positioning of the meteorite collector and the ice sampler. Consequently, for almost all regions where meteorites were found, a correlated surface blue ice sample was collected (Figs. 4a and 5b).

At every collection site the upper 3–5 cm of surface ice were removed (cf. Spaulding et al., 2013), after which the underlying ice was crushed and collected in 60 ml containers. The samples were subsequently transported in liquid phase to the *Analytical, Environmental and Geo- Chemistry* (AMGC) stable isotope laboratory at the *Vrije Universiteit*

*Brussel* (VUB, Belgium). As the containers were sealed, the isotopic fractionation during the time between original collection and analysis was limited, and the original isotopic signal was therefore maintained. The isotopic  $\delta^{18}\text{O}$  and  $\delta\text{D}$  compositions of the 185 samples were simultaneously determined using a Picarro L2130-i Cavity Ring-Down Spectrometer ( $2\sigma$  measurement uncertainty of  $\pm 0.1\text{‰}$  for  $\delta^{18}\text{O}$  and  $\pm 0.5\text{‰}$  for  $\delta\text{D}$ ). Replicates were analysed, and all values were corrected with respect to laboratory standards. These standards span a wide range of isotopic values and were previously calibrated against reference materials from the International Atomic Energy Agency (IAEA). The uncertainty on the individual isotopic measurements ( $\sigma$ ) are on average  $0.10\text{‰}$  for  $\delta^{18}\text{O}$  and  $0.83\text{‰}$  for  $\delta\text{D}$ , which is about one to two order of magnitudes lower than the isotopic variations considered in our study (typically a few ‰ for  $\delta^{18}\text{O}$ ). Note that in the text only the  $\delta^{18}\text{O}$  values are described (these absolute values and associated uncertainties are also added as supplementary material; see Appendix E); but that the  $\delta\text{D}$  values have a similar spatial pattern (Fig. A.1).

## APPENDIX B. TERRESTRIAL AGE DETERMINATION OF SELECTED METEORITES

If a meteorite is assumed to reach the surface and enter the ice sheet in the accumulation area (the source area, t1 on Fig. 1a), to be transported within the ice (t2), to reappear at the surface (in the blue ice area, i.e. the meteorite stranding zone, at t3) and to subsequently move along with the surface flow, then the terrestrial age of the meteorite can be used as a younger limit estimate for the age of the local ice. The age difference between the ice and the terrestrial age of the meteorite results from the surface ablation that occurs between the time of appearance at the surface (t3) and the collection time (somewhere between t3 and t4), which exposes older ice (see Folco et al., 2006 for a detailed account). In this study, the terrestrial age of meteorites was determined by radiocarbon ( $^{14}\text{C}$ ) dating and  $^{36}\text{Cl}$  dating (see Table B1).

All  $^{14}\text{C}$  terrestrial age determinations of meteorites were performed at the University of Arizona AMS Laboratory (United States of America), as described by Jull et al. (1993, 2010). Samples were crushed, pre-treated with 85% phosphoric acid to remove weathering products, washed in distilled water and dried. The meteorite powder ( $\sim 0.2$ – $0.4$  g) was mixed with  $\sim 3$  g of iron chips, which are a combustion accelerator. The mixture was placed in a ceramic crucible and preheated to  $500^\circ\text{C}$  to remove organic contaminants. The crucible was then placed in an RF furnace (Jull et al., 1993) and the sample was heated to melting point for 2 minutes in a flow of oxygen. The recovered gases were passed through a CuO-CeO furnace to ensure conversion to  $\text{CO}_2$  and recovered from the oxygen flow cryogenically.  $\text{CO}_2$  was converted to graphite using standard methods at the Arizona AMS Laboratory and measured by accelerator mass spectrometry. The uncertainty on the terrestrial ages accounts for the uncertainty in the saturated activity and an estimated 3-sigma uncertainty in the blank values.

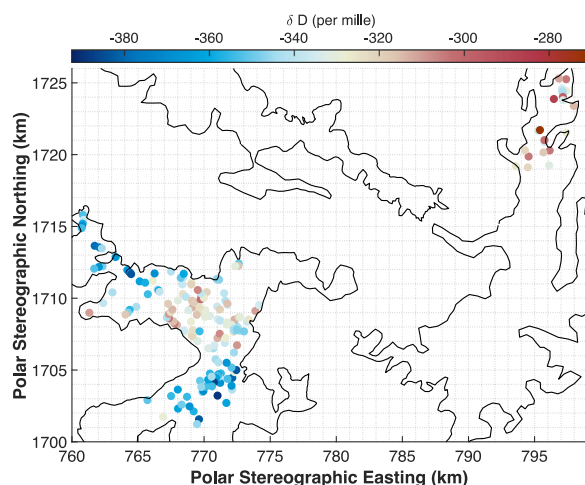


Fig. A1.  $\delta\text{D}$  values of ice samples collected on Nansen blue ice field. The black lines are the outlines of the ice fields.

Table B1

Radiocarbon ( $^{14}\text{C}$ ) dated terrestrial age of meteorites and technical details from measurements.

Meteorite sample	Sample weight (g)	Fm	$\text{CO}_2$ (cc)	Diluted (cc)	$^{14}\text{C}$ atoms	$^{14}\text{C}/\text{g}$	dpm/kg	Saturated Activity	Age (ka)
A 12084	0.413	$2.347 \pm 0.012$	0.355	0.355	$2.279\text{E}+07$	$5.519\text{E}+07$	$12.70 \pm 0.09$	46.4	$10.7 \pm 2.2$
A 12105	0.269	$0.445 \pm 0.016$	0.138	0.138	$5.591\text{E}+05$	$2.078\text{E}+06$	$0.48 \pm 0.09$	46.4	$37.8 \pm 2.6$
A 12324	0.241	$0.334 \pm 0.009$	0.087	0.087	$-3.729\text{E}+05$	$-1.547\text{E}+06$	$-0.36 \pm 0.1$	51.1	>43
A 12326	0.376	$0.407 \pm 0.011$	0.082	0.082	$-2.486\text{E}+05$	$-6.611\text{E}+05$	$-0.15 \pm 0.06$	51.1	>46
A 12389	0.18297	$1.659 \pm 0.01$	0.162	0.162	$6.532\text{E}+06$	$3.570\text{E}+07$	$8.22 \pm 0.14$	55.2	$15.8 \pm 2.4$
A 12430	0.31801	$35.15 \pm 0.33$	0.096	0.096	$9.600\text{E}+07$	$3.019\text{E}+08$	$69.46 \pm 0.66$	55.2	<2.4

Table B2

Concentration of  $^{36}\text{Cl}$  in the metal fraction and derived terrestrial ages.

Meteorite sample	Dissolved metal (mg)	$^{36}\text{Cl}$ concentration (dpm/kg)	Age (ka)
A 12127	12.7	$21.71 \pm 0.73$	<51.2
A 12216	184.9	$17.21 \pm 0.40$	$129.3 \pm 27.9$
A 12324	27.2	$20.24 \pm 0.56$	$48.9 \pm 30.2$
A 12326	83.3	$19.48 \pm 0.55$	$65.5 \pm 30.5$

The  $^{36}\text{Cl}$  terrestrial ages were measured at the ASTER AMS national facility at CEREGE (France). Results are compiled in Table B2. The metal was dissolved in  $\text{HNO}_3$ . After addition of  $^{35}\text{Cl}$  carrier solution ( $^{36}\text{Cl}/^{35}\text{Cl}$  ratio of  $2.96 \cdot 10^{-15} \pm 5.5 \cdot 10^{-16}$ , and a total Cl concentration of 6.92 mg/g), Cl was separated as AgCl. All  $^{36}\text{Cl}$  concentrations were normalized to the KNSTD1600 standard with an assigned  $^{36}\text{Cl}/^{35}\text{Cl}$  ratio of  $2.112 \pm 0.038 \cdot 10^{-12}$  (Fifield et al., 1990; Sharma et al., 1990). Uncertainties (1 sigma) include the uncertainties in the AMS measurements of samples and standards, as well as the  $^{36}\text{Cl}$  content measured in an associated chemistry blank sample. Terrestrial ages were computed using a saturation  $^{36}\text{Cl}$  concentration of  $23.18 \pm 1.35$  dpm/kg for H chondrites,  $22.65 \pm 0.95$  dpm/kg for L chondrites. These saturation values were computed using  $^{36}\text{Cl}$  concentrations measured in the metal of 18 H falls (Graf et al., 2001; Dalcher et al., 2013) and 10 L falls (Dalcher et al., 2013). For the LL chondrite, we used the L chondrite saturation value ( $22.65 \pm 0.95$  dpm/kg).

### APPENDIX C. ICE DYNAMIC 1-D FLOWLINE MODEL

Ice sheets are characterized by a small ratio between the ice thickness and the horizontal scales. To describe the ice flow in their interior regions (i.e. away from the coast), the shallow-ice approximation (SIA) is commonly used (Hutter, 1983). In the SIA, the ice flow is assumed to be entirely driven by vertical gradients in shearing. For ice flow along a flowline (1-D), the depth-averaged velocity is given by:

$$\bar{u} = AH\tau^3 \quad (\text{C.1})$$

where  $H$  is the ice thickness (m),  $A$  is the rate factor ( $\text{Pa}^{-3} \text{a}^{-1}$ ), and  $\tau$  is the driving stress (Pa):

$$\tau = -\rho g H \frac{\partial h}{\partial x} \quad (\text{C.2})$$

Here,  $\rho$  is the density of ice ( $910 \text{ kg m}^{-3}$ ),  $g$  is the gravitational acceleration ( $9.81 \text{ m s}^{-2}$ ) and  $\frac{\partial h}{\partial x}$  is the surface slope (unitless).

These equations can be used to estimate the magnitude of the ice flow surface velocities on the Nansen ice field. The ice thickness ( $H$ ) is estimated to be around 1000 m (see Section 5), while the surface slope ( $\frac{\partial h}{\partial x}$ ) along the ice flow direction (i.e. perpendicular to the elevation contours) is close to 1% (130 m over a distance of 12 km for Nansen B). The main unknown is the rate factor ( $A$ ), which is strongly dependent on the ice temperature. In ice flow modelling studies, this relationship is typically described through an Arrhenius-type law (e.g. Huybrechts et al., 2011; Pollard and Deconto, 2012; Seddik et al., 2012; Zekollari et al., 2017a; Hindmarsh, 2018):

$$A = A_0 e^{-Q/RT} \quad (\text{C.3})$$

where  $A_0$  is a constant ( $1.14 \times 10^{-5} \text{ Pa}^{-3} \text{a}^{-1}$  for  $T < -10^\circ\text{C}$ ;  $5.47 \times 10^{10} \text{ Pa}^{-3} \text{a}^{-1}$  for  $T > -10^\circ\text{C}$ ),  $Q$  is the activation energy for creep ( $60 \text{ kJ mol}^{-1}$  for  $T < -10^\circ\text{C}$ ;  $139 \text{ kJ mol}^{-1}$  for  $T > -10^\circ\text{C}$ ),  $R$  is the universal gas constant ( $8.314 \text{ J mol}^{-1} \text{K}^{-1}$ ) and  $T$  is the temperature relative to the melting point (K).

For the Nansen ice field, the ice temperatures at the base of the ice sheet are expected to be close to the pressure melting point (Van Liefferinge and Pattyn, 2013; Van Liefferinge et al., 2018). Close to the surface the ice temperatures approximate the mean annual air temperature, which is around  $-40^\circ\text{C}$ . Most of the deformation occurs in the lower parts of the ice column, where ice temperatures are the highest, and we therefore consider depth-averaged rates factors between  $2.7 \times 10^{-17}$  (corresponding to  $-25^\circ\text{C}$ ) and  $1.47 \times 10^{-18}$  (corresponding to  $-10^\circ\text{C}$ ) to be realistic. By relying on this spread in rate factors and by accounting for a possible spread in ice thicknesses around the ca. 1000 m thickness obtained from a few airborne flight lines (Eagles et al., 2018) (see Section 5), depth-averaged

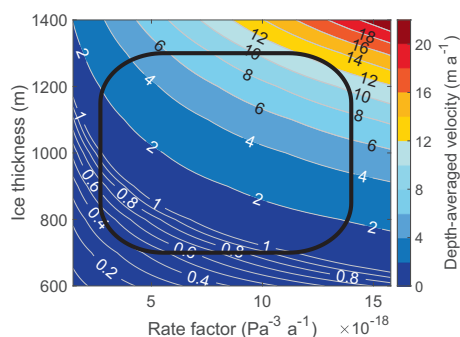


Fig. C1. Depth-averaged velocity estimation for the Nansen blue ice field ( $\frac{\partial h}{\partial x} = 0.011$ ), as a function of varying rate factors ( $A$ ) and ice thicknesses ( $H$ ). The black box delineates the plausible range for the rate factor and the ice thickness.

velocities in the order of 0.4–12 m a<sup>−1</sup> are typically expected over the Nansen ice field (Fig. C.1).

#### APPENDIX D. SURFACE MASS BALANCE MODELLING

To estimate the ablation (negative SMB) over the Nansen blue ice field, we used a surface energy balance (SEB) model (van den Broeke et al., 2006, 2010; Kuipers Munneke et al., 2018), driven by Automatic Weather Station (AWS) measurements at Kohnen. This AWS is situated at the EPICA ice core site, at 75°S, 0°E, 3000 m a.s.l. (Van As et al., 2007; Medley et al., 2018). As Kohnen is not located in a blue ice area, but elevation is similar to that of the Nansen blue ice field, we used the observed meteorology apart from resetting the surface albedo to a constant

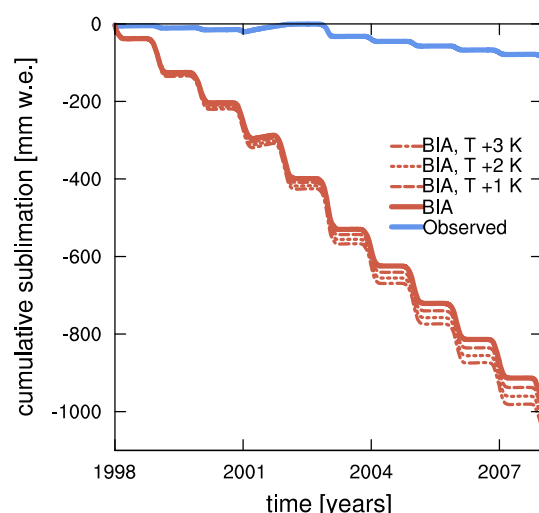


Fig. D1. Cumulative (1998–2007, i.e. 10 years) surface sublimation at Kohnen station as derived from AWS observations and an SEB model, using the observed surface albedo (blue), blue ice albedo (red), and blue ice albedo with increased near-surface temperatures (red dotted lines, see legend). (For interpretation of the references to colour in this figure legend, the reader is referred to the web version of this article.)

value, which is typical for Antarctic blue ice (0.57, Lenaerts et al., 2017).

Hereby we assumed that all the accumulated snow instantaneously sublimates or is eroded, and blue ice is exposed at the surface at all times. Without accumulation, (negative) SMB is dominated by surface mass loss through surface sublimation, which can be estimated using the SEB model. Fig. D.1 shows that sublimation is small when using the observed albedo, but amounts to about 100 mm w.e. a<sup>−1</sup> when the blue ice albedo is applied. To test the sensitivity of the results for higher near-surface temperatures above blue ice relative to over snow surfaces (Bintanja and van den Broeke, 1995), we performed three additional SEB model simulations with 1, 2 and 3 K higher temperatures. The results of these sensitivity tests show that sublimation increases slightly with increasing temperatures (up to 10% with a 3 K temperature increase), but the differences remain relatively small. This indicates that the result is relatively robust, and suggests that annual SMB over the Nansen blue ice field is around −100 mm w.e. a<sup>−1</sup>. By accounting for model uncertainties (e.g. ice albedo, possible spatial variations in melt, ... etc.), it is estimated that the annual SMB over the Nansen ice field is between −125 and −75 mm w.e. a<sup>−1</sup>.

Outside of the Nansen ice field, SMB is positive and dominated by snowfall. Without in-situ SMB observations, we rely on output of the well-evaluated regional atmospheric climate model RACMO2 (updated from Lenaerts et al., 2017) at a high spatial resolution (5.5 km) to provide an estimate of regional SMB. An earlier version of this model (Van Wessem et al., 2014), run at lower resolution

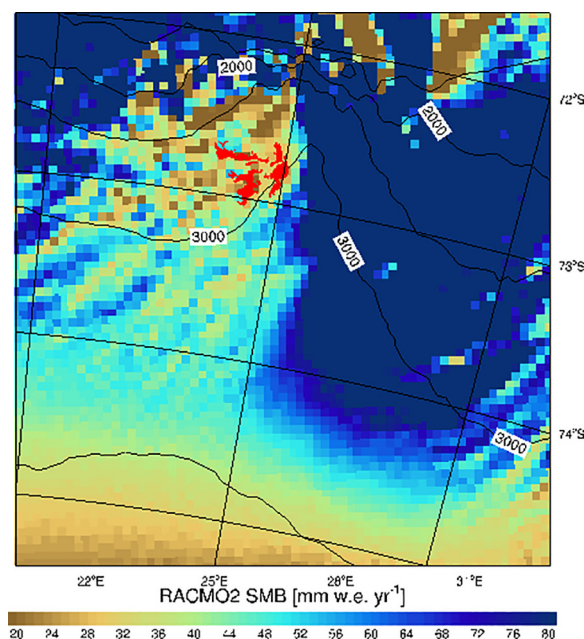


Fig. D2. Annual mean (1979–2016) SMB simulated by RACMO2 at a 5.5 km resolution (updated from Lenaerts et al., 2017). The red area shows the location of the Nansen ice field. (For interpretation of the references to colour in this figure legend, the reader is referred to the web version of this article.)



(27 km), proved to reproduce measured SMBs well in and around the Sør Rondane mountains (Callens et al., 2015). Fig. D.2 shows that the simulated annual SMB amounts to 20–50 mm w.e. in a wide area south and southwest of the Nansen blue ice field.

## APPENDIX E. SUPPLEMENTARY MATERIAL

Supplementary data associated with this article can be found, in the online version, at <http://dx.doi.org/10.1016/j.gca.2017.07.013>.

The  $\delta^{18}\text{O}$  values of the surface blue ice samples with associated uncertainties ( $1\sigma$ ) are available as supplementary material. The supplementary material also includes a picture of every newly dated meteorite (from the 2012/13 expedition) at the collection site.

## REFERENCES

- Bader N. A., Licht K. J., Kaplan M. R., Kassab C. and Winckler G. (2017) East Antarctic ice sheet stability recorded in a high-elevation ice-cored moraine. *Quat. Sci. Rev.* **159**, 88–102. <https://doi.org/10.1016/j.quascirev.2016.12.005>.
- Basile I., Petit J. R., Touron S., Grousset F. E. and Barkov N. (2001) Volcanic layers in Antarctic (Vostok) ice cores: source identification and atmospheric implications. *J. Geophys. Res.* **106**, 31915–31931. <https://doi.org/10.1029/2000JD000102>.
- Benoit P. H. (1995) Meteorites as surface exposure time markers on the blue ice fields of Antarctica: episodic ice flow in Victoria land over the last 300,000 years. *Quat. Sci. Rev.* **14**, 531–540. [https://doi.org/10.1016/0277-3791\(95\)00011-D](https://doi.org/10.1016/0277-3791(95)00011-D).
- Benoit P. H., Sears D. W. G., Akridge J. M. C., Bland P. A., Berry F. J. and Pillinger C. T. (2000) The non-trivial problem of meteorite pairing. *Meteorit. Planet. Sci.* **35**, 393–417. <https://doi.org/10.1111/j.1945-5100.2000.tb01785.x>.
- Bentley M. J., Cofaigh C. Ó., Anderson J. B., Conway H., Davies B., Graham A. G. C., Hillenbrand C., Hodgson D. A., Jamieson S. S. R., Larter R. D., Mackintosh A., Smith J. A., Verleyen E., Ackert R. P., Bart P. J., Berg S., Brunstein D., Canals M., Colhoun E. A., Crosta X., Dickens W. A., Domack E., Dowdeswell J. A., Dunbar R., Ehrmann W., Evans J., Favier V., Fink D., Fogwill C. J., Glasser N. F., Gohl K., Golledge N. R., Goodwin I., Gore D. B., Greenwood S. L., Hall B. L., Hall K., Hedding D. W., Hein A. S., Hocking E. P., Jakobsson M., Johnson J. S., Jomelli V., Jones R. S., Klages J. P., Kristoffersen Y., Kuhn G., Leventer A., Licht K., Lilly K., Lindow J., Mcglone M. S., McKay R. M., Livingstone S. J., Mass G., Melles M., Miura H., Mulvaney R., Nel W., Nitsche F. O., Brien P. E. O., Post A. L., Roberts S. J., Saunders K. M., Selkirk P. M., Simms A. R., Spiegel C., Stollendorf T. D., Sugden D. E., van der Putten N., van Ommen T., Verfaillie D., Vyverman W., Wagner B., White D. A., Witus A. E. and Zwartz D. (2014) A community-based geological reconstruction of Antarctic Ice Sheet deglaciation since the Last Glacial Maximum. *Quat. Sci. Rev.* **100**, 1–9. <https://doi.org/10.1016/j.quascirev.2014.06.025>.
- Bibby T., Putkonen J., Morgan D., Balco G. and Shuster D. L. (2016) Million year old ice found under meter thick debris layer in Antarctica. *Geophys. Res. Lett.* **6995–7001**. <https://doi.org/10.1002/2016GL069889>. Received.
- Bindschadler R., Vornberger P., Fleming A., Fox A., Mullins J., Binnie D., Paulsen S. J., Granneman B. and Gorodetzky D. (2008) The Landsat image mosaic of Antarctica. *Remote Sens. Environ.* **112**, 4214–4226. <https://doi.org/10.1016/j.rse.2008.07.006>.
- Bintanja R. (1999) On the glaciological, meteorological, and climatological significance of Antarctic blue ice areas. *Rev. Geophys.* **37**, 337–359. <https://doi.org/10.1029/1999RG900007>.
- Bintanja R. and van den Broeke M. R. (1995) The surface energy balance of Antarctic snow and blue ice. *J. Appl. Meteorol.* **34**, 902–926.
- Bland P. A. (2001) Quantification of Meteorite Infall Rates from Accumulations in Deserts, and Meteorite Accumulations on Mars. In (Eds. B. Peucker-Ehrenbrink and B. Schmitz), *Accretion of Extraterrestrial Matter Throughout Earth's History*. Springer US, Boston, MA. pp. 267–303. doi: 10.1007/978-1-4419-8694-8\_15.
- Buizert C., Baggenstos D., Jiang W., Purtschert R., Petrenko V. V., Lu Z.-T., Müller P., Kuhl T., Lee J., Severinghaus J. P. and Brook E. J. (2014) Radiometric  $^{81}\text{Kr}$  dating identifies 120,000-year-old ice at Taylor Glacier, Antarctica. *Proc. Natl. Acad. Sci. USA* **111**, 6876–6881. <https://doi.org/10.1073/pnas.1320329111>.
- Callens D., Matsuoka K., Steinhage D., Smith B., Wittrant E. and Pattyn F. (2014) Transition of flow regime along a marine-terminating outlet glacier in East Antarctica. *Cryosphere* **8**, 867–875. <https://doi.org/10.5194/tc-8-867-2014>.
- Callens D., Thonnard N., Lenaerts J. T. M., van Wessem J. M., van de Berg W. J., Matsuoka K. and Pattyn F. (2015) Mass balance of the Sør Rondane glacial system, East Antarctica. *Ann. Glaciol.* **56**, 63–69. <https://doi.org/10.3189/2015AoG70A010>.
- Cassidy W., Harvey R., Schutt J., Delisle G. and Yanai K. (1992) The meteorite collection sites of Antarctica. *Meteoritics* **27**, 490–525. <https://doi.org/10.1111/j.1945-5100.1992.tb01073.x>.
- Corti G., Zeoli A., Belmaggio P. and Folco L. (2008) Physical modeling of the influence of bedrock topography and ablation on ice flow and meteorite concentration in Antarctica. *J. Geophys. Res. Earth Surf.* **113**, F01018. <https://doi.org/10.1029/2006JF000708>.
- Corti G., Zeoli A. and Bonini M. (2003) Ice-flow dynamics and meteorite collection in Antarctica. *Earth Planet. Sci. Lett.* **215**, 371–378. [https://doi.org/10.1016/S0012-821X\(03\)00440-0](https://doi.org/10.1016/S0012-821X(03)00440-0).
- Curzio P., Folco L., Laurenzi M. A., Mellini M. and Zeoli A. (2008) A tephra chronostratigraphic framework for the Frontier Mountain blue-ice field (northern Victoria Land, Antarctica). *Quat. Sci. Rev.* **27**, 602–620.
- Dalcher N., Caffee M. W., Nishiizumi K., Welten K. C., Vogel N., Wieler R. and Leya I. (2013) Calibration of cosmogenic noble gas production in ordinary chondrites based on  $^{36}\text{Cl}$ – $^{36}\text{Ar}$  ages. Part 1: refined produced rates for cosmogenic  $^{21}\text{Ne}$  and  $^{38}\text{Ar}$ . *Meteorit. Planet. Sci.* **48**, 1841–1862. <https://doi.org/10.1111/maps.12203>.
- Debaille V., Imae N., Yamaguchi A., Goderis S., Mikouchi T., Debouge W., Hublet G., Van Roosbroek N., Zekollari H., Kojima H. and Claeys P. (2013) The 2012–2013 joint field campaign for collecting meteorites in Antarctica: an efficient collaboration between Japan and Belgium. *Antarct. Meteorites XXXVI* 11–12.
- Delisle G., Franchi I., Rossi A. and Wieler R. (1993) Meteorite finds by EUROMET near Frontier Mountain, North Victoria Land, Antarctica. *Meteoritics* **28**, 126–129.
- Eagles G., Karlsson N. B., Ruppel A., Steinhage D., Jokati W. and Läufer A. (2018) Erosion at extended continental margins: Insights from new aerogeophysical data in eastern Dronning Maud Land. *Gondwana Res.* **63**, 105–116.
- Eppler D. B. (2011) Analysis of Antarctic logistics and operations data: Results from the Antarctic Search for Meteorites

- (ANSMET), austral summer season, 2002–2003, with implications for planetary surface operations. *Geol. Soc. Am.* **75**–84. [https://doi.org/10.1130/2011.2483\(06\)](https://doi.org/10.1130/2011.2483(06)).
- Fahnestock M., Scambos T., Moon T., Gardner A., Haran T. and Klinger M. (2016) Remote sensing of environment rapid large-area mapping of ice flow using Landsat 8. *Remote Sens. Environ.* **185**, 84–94. <https://doi.org/10.1016/j.rse.2015.11.023>.
- Faure G., Hagen E. H., Johnson K. S. and Buchanan D. (1993) Profile of oxygen isotope compositions of ice in the Lewis Cliff ice tongue, Transantarctic Mountains. *Antarct. J. United States*, 69–70.
- Fifield L. K., Ophel T. R., Allan G. L., Bird J. R. and Davie R. F. (1990) Accelerator mass spectrometry at the Australian National University's 14UD accelerator: experience and developments. *Nucl. Instrum. Methods Phys. Res. B* **52**, 233–237.
- Folco L., Capra A., Chiappini M., Frezzotti M., Mellini M. and Tabacco I. E. (2002) The Frontier Mountain meteorite trap (Antarctica). *Meteorit. Planet. Sci.* **37**, 209–228. <https://doi.org/10.1017/CBO9781107415324.004>.
- Folco L., Orazio M. D., Gemelli M. and Rochette P. (2016) Stretching out the Australasian microtektite strewn field in Victoria Land Transantarctic Mountains. *Polar Sci.* **10**, 147–159. <https://doi.org/10.1016/j.polar.2016.02.004>.
- Folco L., Welten K. C., Jull A. J. T., Nishiizumi K. and Zeoli A. (2006) Meteorites constrain the age of Antarctic ice at the Frontier Mountain blue ice field (northern Victoria Land). *Earth Planet. Sci. Lett.* **248**, 194–201. <https://doi.org/10.1016/j.epsl.2006.05.022>.
- Fretwell P., Pritchard H. D., Vaughan D. G., Bamber J. L., Barrand N. E., Bell R., Bianchi C., Bingham R. G., Blankenship D. D., Casassa G., Catania G., Callens D., Conway H., Cook A. J., Corr H. F. J., Damaske D., Damm V., Ferraccioli F., Forsberg R., Fujita S., Gim Y., Gogineni P., Griggs J. A., Hindmarsh R. C. A., Holmlund P., Holt J. W., Jacobel R. W., Jenkins A., Jokat W., Jordan T., King E. C., Kohler J., Krabill W., Riger-Kusk M., Langley K. A., Leitchenkov G., Leuschen C., Luyendyk B. P., Matsuoka K., Mougnot J., Nitsche F. O., Nogi Y., Nost O. A., Popov S. V., Rignot E., Rippin D. M., Rivera A., Roberts J., Ross N., Siegert M. J., Smith A. M., Steinhage D., Studinger M., Sun B., Tinto B. K., Welch B. C., Wilson D., Young D. A., Xiangbin C. and Zirizzotti A. (2013) Bedmap 2: Improved ice bed, surface and thickness datasets for Antarctica. *Cryosph.* **7**, 375–393. <https://doi.org/10.5194/tc-7-375-2013>.
- Fujita S., Parrenin F., Severi M., Motoyama H. and Wolff E. W. (2015) Volcanic synchronization of Dome Fuji and Dome C Antarctic deep ice cores over the past 216 kyr. *Clim. Past* **11**, 1395–1416. <https://doi.org/10.5194/cp-11-1395-2015>.
- Gardner A. S., Moholdt G., Scambos T., Fahnestock M., Ligtenberg S., van den Broeke M. and Nilsson J. (2018) Increased West Antarctic and unchanged East Antarctic ice discharge over the last 7 years. *Cryosph.* **12**, 521–547. <https://doi.org/10.5194/tc-12-521-2018>.
- Genge M. J., Ginneken M. V. A. N., Suttle M. D. and Harvey R. P. (2018) Accumulation mechanisms of micrometeorites in an ancient supraglacial moraine at Larkman Nunatak, Antarctica. *Meteorit. Planet. Sci.* **53**, 2051–2066. <https://doi.org/10.1111/maps.13107>.
- Goderis S., Kaiden H., Debaille V., Kojima H. and Claeys P. (2011) Belgian-Japanese search for Antarctic meteorites during the 2010–2011 field season. In *Antarctic Meteorites XXXIV*. Tokyo, p. 12.
- Goelzer H., Huybrechts P., Raper S. C. B., Loutre M.-F., Goosse H. and Fichet T. (2012) Millennial total sea-level commitments projected with the Earth system model of intermediate complexity LOVECLIM. *Environ. Res. Lett.* **7**, 045401. <https://doi.org/10.1088/1748-9326/7/4/045401>.
- Graf T., Caffee M. W., Marti K., Nishiizumi K. and Pongonis K. V. (2001) Dating collisional events:  $^{36}\text{Cl}$ – $^{36}\text{Ar}$  exposure ages of H-chondritic metals. *Icarus* **150**, 181–188. <https://doi.org/10.1006/icar.2000.6560>.
- Graly J. A., Licht K. J., Kassab C. M., Bird B. W. and Kaplan M. R. (2018) Warm-based basal sediment entrainment and far-field Pleistocene origin evidenced in central Transantarctic blue ice through stable isotopes and internal structures. *J. Glaciol.* **64**, 185–196. <https://doi.org/10.1017/jog.2018.4>.
- Grinsted A., Moore J., Spikes V. B. and Sinisalo A. (2003) Dating Antarctic blue ice areas using a novel ice flow model. *Geophys. Res. Lett.* **30**, 2005. <https://doi.org/10.1029/2003GL017957>.
- Halliday I., Blackwell A. T. and Griffin A. A. (1989) The flux of meteorites on the Earth's surface. *Meteoritics* **24**, 173–178.
- Harvey R. (2003) The origin and significance of antarctic meteorites. *Chemie der Erde – Geochemistry* **63**, 93–147. <https://doi.org/10.1078/0009-2819-00031>.
- Harvey R.P., Schutt J. and Karner J. (2015) Fieldwork Methods of the U.S. Antarctic Search for Meteorites Program. In (Eds. K. Righter, C. M. Corrigan, T. J. McCoy, R. P. Harvey), 35 Seasons of the U.S. Antarctic Meteorites (1976–2010): A Pictorial Guide to the Collection. American Geophysical Union and John Wiley & Sons, Inc., Washington. pp. 23–41.
- Herzog G. F., Caffee M. W. and Jull T. A. J. (2015) Cosmogenic nuclides in antarctic meteorites. In: (Eds. K. Righter, C.M. Corrigan, T.J. McCoy, R.P. Harvey), 35 Seasons of the U.S. Antarctic (1976–2010): A Pictorial Guide to the Collection. American Geophysical Union and John Wiley & Sons, Inc., Washington. pp. 153–172.
- Higgins J. A., Kurbatov A. V., Spaulding N. E., Brook E., Introne D. S., Chimiak L. M., Yan Y., Mayewski P. A. and Bender M. L. (2015) Atmospheric composition 1 million years ago from blue ice in the Allan Hills Antarctica. *Proc. Natl. Acad. Sci.* **112**, 6887–6891. <https://doi.org/10.1073/pnas.1420232112>.
- Hindmarsh R.C.A. (2018) Ice Sheet and Glacier Modelling. In *Past Glacial Environments*. Elsevier Ltd, pp. 605–661. doi: 10.1016/B978-0-08-100524-8.00019-1.
- Huss G. R. (1990) Meteorite infall as a function of mass: implications for the accumulation of meteorites on Antarctic ice. *Meteoritics* **25**, 41–56. <https://doi.org/10.1111/j.1945-5100.1990.tb00969.x>.
- Hutter K. (1983) *Theoretical Glaciology*. Reidel Publ. Co., Dordrecht.
- Huybrechts P., Goelzer H., Janssens I., Driesschaert E., Fichet T., Goosse H. and Loutre M. F. (2011) Response of the Greenland and Antarctic ice sheets to multi-millennial greenhouse warming in the earth system model of intermediate complexity LOVECLIM. *Surv. Geophys.* **32**, 397–416. <https://doi.org/10.1007/s10712-011-9131-5>.
- Huybrechts P., Rybak O., Pattyn F., Ruth U. and Steinhage D. (2007) Ice thinning, upstream advection, and non-climatic biases for the upper 89% of the EDML ice core from a nested model of the Antarctic ice sheet. *Clim. Past* **3**, 577–589. <https://doi.org/10.5194/cpd-3-693-2007>.
- Ikeda Y. and Kimura M. (1992) Mass distribution of Antarctic ordinary chondrites and the estimation of the fall-to-specimen ratios. *Meteoritics* **27**, 435–441.
- Imae N., Akada Y., Berclaz C., Claeys P., Debaille V., Goderis S., Hublet G., Kojima H., Mikouchi T., Van Roosbroek N., Debouge W., Yamaguchi A. and Zekollari H. (2013) The search for Antarctic meteorites in the Nansen Ice Field by the joint team of Japan and Belgium. In *Proc. Japan Geosci. Union Meet. PPS24-P05*.

- Imae N., Debaille V., Akada Y., Debouge W., Goderis S., Hublet G., Mikouchi T., Van Roosbroek N., Yamaguchi A., Zekollari H., Claeys P. and Kojima H. (2015) Report of the JARE-54 and BELARE 2012–2013 joint expedition to collect meteorites on the Nansen Ice Field, Antarctica. *Antarct. Rec.* **59**, 38–72.
- Jacobs J., Opås B., Elburg M. A., Läufer A., Estrada S., Ksienzyk A. K., Damaske D. and Hofmann M. (2017) Cryptic sub-ice geology revealed by a U-Pb zircon study of glacial till in Dronning Maud Land, East Antarctica. *Precambrian Res.* **294**, 1–14. <https://doi.org/10.1016/j.precamres.2017.03.012>.
- Jouzel J., Vimeux F., Caillon N., Delaygue G., Hoffmann G. and Parrenin F. (2003) Magnitude of isotope/temperature scaling for interpretation of central Antarctic ice cores. *J. Geophys. Res.* **108**, 4361. <https://doi.org/10.1029/2002JD002677>.
- Jull A. J. T., Donahue D. J., Cielaszyk E. and Wlotzka F. (1993) Carbon-14 terrestrial ages and weathering of 27 meteorites from the southern high plains and adjacent areas (USA). *Meteoritics* **28**, 188–195.
- Jull A. J. T., McHargue L. R., Bland P. A., Greenwood R. C., Bevan A. W. R., Kim K. J., Giscard M. D., LaMotta S. E. and Johnson J. A. (2010) Terrestrial  $^{14}\text{C}$  and  $^{14}\text{C}$ – $^{10}\text{Be}$  ages of meteorites from the Nullarbor, Australia. *Meteorit. Planet. Sci.* **45**, 1271–1283.
- Jull T.A.J. (2006) Terrestrial ages of meteorites. In *Meteorites and the Early Solar System II*. pp. 889–905. doi: 10.1038/293433a0.
- Kamb B. and Echelmayer K. A. (1986) Stress-Gradient Coupling in Glacier Flow: I. Longitudinal Averaging of the Influence of Ice Thickness and Surface Slope. *J. Glaciol.* **32**, 267–284. <https://doi.org/10.3198/1986JoG32-111-285-298>.
- Kaplan M. R., Licht K. J., Winckler G., Schaefer J. M., Bader N., Mathieson C., Roberts M., Kassab C. M., Schwartz R. and Graly J. A. (2017) Middle to Late Pleistocene stability of the central East Antarctic Ice Sheet at the head of Law Glacier. *Geology* **45**, 963–966. <https://doi.org/10.1130/G39189.1>.
- Kehrl L., Conway H., Holschuh N., Campbell S., Kurbatov A. V. and Spaulding N. E. (2018) Evaluating the duration and continuity of potential climate records from the Allan Hills Blue Ice Area, East Antarctica. *Geophys. Res. Lett.* **45**, 4096–4104.
- Koeberl C. and Cassidy W. A. (1991) Differences between Antarctic and non-Antarctic meteorites: an assessment. *Geochim. Cosmochim. Acta* **55**, 3–18.
- Kohno M., Fujii Y. and Hirata T. (2004) Chemical composition of volcanic glasses in visible tephra layers found in a 2503 m deep ice core from Dome Fuji, Antarctica. *Ann. Glaciol.* **39**, 576–584.
- Kuipers Munneke P., Smeets C. J. P. P., Reijmer C. H., Oerlemans J., van de Wal R. S. W. and van den Broeke M. R. (2018) The K-transect on the western Greenland Ice Sheet: surface energy balance (2003–2016). *Arct. Antarct. Alp. Res.* **50**, e1420952. <https://doi.org/10.1080/15230430.2017.1420952>.
- Lenaerts J. T. M., Lhermitte S., Drews R., Ligtenberg S. R. M., Berger S., Helm V., Smeets P. C. J. P., van den Broeke M. R., van De Berg W. J., van Meijgaard E., Eijkelboom M., Eisen O. and Pattyn F. (2017) Meltwater produced by wind – albedo interaction stored in an East Antarctic ice shelf. *Nat. Clim. Change* **7**, 58–63. <https://doi.org/10.1038/NCLIMATE3180>.
- Licht K. J. and Hemming S. R. (2017) Analysis of Antarctic glacial sediment provenance through geochemical and petrologic applications. *Quat. Sci. Rev.* **164**, 1–24. <https://doi.org/10.1016/j.quascirev.2017.03.009>.
- Lindstrom M.M., Score R. (1995) Populations, pairing and rare meteorites in the U.S. Antarctic meteorite collection. In (Eds. L. Schultz, J.O. Annestad, M.E. Zolensky), Workshop on Meteorites from Cold and Hot Deserts. LPI Technical Report 95-02, Lunar and Planetary Institute, Houston, pp. 43–45.
- Mackintosh A. N., Verleyen E., Brien P. E. O., White D. A., Jones R. S., McKay R., Dunbar R., Gore D. B., Fink D., Post A. L., Miura H., Leventer A., Goodwin I., Hodgson D. A., Lilly K., Crosta X., Golledge N. R., Wagner B., Berg S., van Ommen T., Zwartz D., Roberts S. J., Vyverman W. and Masse G. (2014) Retreat history of the East Antarctic Ice Sheet since the Last Glacial Maximum. *Quat. Sci. Rev.* **100**, 10–30. <https://doi.org/10.1016/j.quascirev.2013.07.024>.
- Masson-Delmotte V., Buiron D., Ekaykin A., Frezzotti M., Gallée H., Jouzel J., Krinner G., Landais A., Motoyama H., Oerter H., Pol K., Pollard D., Ritz C., Schlosser E., Sime L. C., Sodemann H., Stenni B., Uemura R. and Vimeux F. (2011) A comparison of the present and last interglacial periods in six Antarctic ice cores. *Clim. Past* **7**, 397–423. <https://doi.org/10.5194/cp-7-397-2011>.
- Masson-Delmotte V., Hou S., Ekaykin A., Jouzel J., Aristarain A., Bernardo R. T., Bromwich D., Cattani O., Delmotte M. M., Falourd S., Frezzotti M., Gallée H., Genoni L., Isaksson E., Landais A., Helsen M. M., Hoffmann G., Lopez J., Morgan V., Motoyama H., Noone D., Oerter H., Petit J. R., Royer A., Uemura R., Schmidt G. A., Schlosser E., Simões J. C., Steig E. J., Stenni B., Stievenard M., van den Broeke M. R., van de Wal R. S. W., van de Berg W. J., Vimeux F. and White J. W. C. (2008) A review of antarctic surface snow isotopic composition: observations, atmospheric circulation, and isotopic modeling. *J. Clim.* **21**, 3359–3387. <https://doi.org/10.1175/2007JCLI2139.1>.
- Medley B., McConnell J. R., Neumann T. A., Reijmer C. H., Chellman N., Sigl M. and Kipfstuhl S. (2018) Temperature and snowfall in Western Queen Maud Land increasing faster than climate model projections. *Geophys. Res. Lett.* **45**, 1472–1480. <https://doi.org/10.1002/2017GL075992>.
- Meteoritical Bulletin Database (2018) Meteoritical Bulletin Database. Available at <<https://www.lpi.usra.edu/meteor>> (accessed on August 8 2018).
- Moore J. C., Nishio F., Fujita S., Narita H., Pasteur E., Grinsted A., Sinisalo A. and Maeno N. (2006) Interpreting ancient ice in a shallow ice core from the South Yamato (Antarctica) blue ice area using flow modeling and compositional matching to deep ice cores. *J. Geophys. Res. Atmos.* **111**, D16302. <https://doi.org/10.1029/2005JD006343>.
- Mouginot J., Rignot E., Scheuchl B. and Millan R. (2017) Comprehensive annual ice sheet velocity mapping using Landsat-8, Sentinel-1, and RADARSAT-2 Data. *Remote Sens.* **9**, 1–20. [https://doi.org/10.1007/978-3-540-74698-0\\_119](https://doi.org/10.1007/978-3-540-74698-0_119).
- Muhs D. R., Aleinikoff J. N., Stafford T. W., Kihl R., Been J., Mahan S. A. and Cowherd S. (1999) Late Quaternary loess in northeastern Colorado: Part I – age and paleoclimatic significance. *Bull. Geol. Soc. Am.* **111**, 1861–1875. [https://doi.org/10.1130/0016-7606\(1999\)111](https://doi.org/10.1130/0016-7606(1999)111).
- Nagao K. and Miura Y. (1993) Noble gases and  $^{81}\text{Kr}$ -terrestrial age of Asuka-881757 lunar Meteorite. *Proc. NIPR Symp. Antarct. Meteorites* **6**, 76–87.
- Nagata T. (1982) Search for Antarctic meteorites. In *Antarctic Geosciences – International Union of Geological Sciences Series B*, Beijing China. pp. 1049–1058.
- Naraoka H., Yanai K. and Fujita S. (1990) Report on Antarctic meteorites search around the Sør Rondane Mountains. *Antarct. Rec.* **34**, 216–224.
- Narcisi B., Petit J. R., Delmonte B., Basile-Doelsch I. and Maggi V. (2005) Characteristics and sources of tephra layers in the EPICA-Dome C ice record (East Antarctica): implications for past atmospheric circulation and ice core stratigraphic correlations. *Earth Planet. Sci. Lett.* **239**, 253–265. <https://doi.org/10.1016/j.epsl.2005.09.005>.



- Ninagawa K., Imae N., Kojima H., Yanai K. and Jull A. J. T. (2006) Thermoluminescence study in the Japanese Antarctic Meteorites Collection: Asuka Ordinary Chondrites. *Meteorit. Planet. Sci.* A132.
- Ninagawa K., Mieda Y., Ueda H., Imae N., Kojima H. and Yanai K. (2005) Thermoluminescence studies of ordinary chondrites in the Japanese Antarctic meteorite collection IV: Asuka ordinary chondrites. *Antarct. Meteor. Res.* **18**, 1–16.
- Nishiizumi K., Arnold J. R., Caffee M. W., Finkel R. C. and Reedy R. C. (1992) Cosmic ray exposure histories of lunar meteorites Asuka-881757, Yamato-793169, and Calalong Creek. *Antarct. Meteorites XVII*, 129–132.
- Nishiizumi K., Elmore D. and Kubik P. W. (1989) Update on terrestrial ages of Antarctic meteorites. *Earth Planet. Sci. Lett.* **93**, 299–313. [https://doi.org/10.1016/0012-821X\(89\)90029-0](https://doi.org/10.1016/0012-821X(89)90029-0).
- Oda H., Miyagi I., Kawai J., Suganuma Y., Funaki M., Imae N., Mikouchi T., Matsuzaki T. and Yamamoto Y. (2016) Volcanic ash in bare ice south of Sør Rondane Mountains, Antarctica: geochemistry, rock magnetism and nondestructive magnetic detection with SQUID gradiometer. *Earth, Planets Sp.* **68**, 1–19. <https://doi.org/10.1186/s40623-016-0415-3>.
- Palais J. M., Petit J. R., Lorus C. and Korotkevich Y. S. (1989) Tephra layers in the Vostok ice core: 160,000 years of southern hemisphere volcanism. *Antarct. J. United States* **24**, 98–100.
- Pattyn F., Favier L., Sun S. and Durand G. (2017) Progress in numerical modeling of Antarctic ice-sheet dynamics. *Curr. Clim. Chang. Reports* **3**, 174–184. <https://doi.org/10.1007/s40641-017-0069-7>.
- Pollard D. and Deconto R. M. (2012) Description of a hybrid ice sheet-shelf model, and application to Antarctica. *Geosci. Model Dev.* **5**, 1273–1295. <https://doi.org/10.5194/gmd-5-1273-2012>.
- Pourkhorsandi H., D'Orazio M., Rochette P., Valenzuela M., Gattacceca J., Mirnejad H., Sutter B., Hutzler A. and Aboulahe M. (2017) Modification of REE distribution of ordinary chondrites from Atacama (Chile) and Lut (Iran) hot deserts: insights into the chemical weathering of meteorites. *Meteorit. Planet. Sci.* **52**, 1843–1858. <https://doi.org/10.1111/maps.12894>.
- Righter K., Corrigan C., McCoy T. and Harvey R. (2015) *35 Seasons of US Antarctic Meteorites (1976–2010): A Pictorial Guide to the Collection*. John Wiley & Sons.
- Rignot E., Mouginot J. and Scheuchl B. (2017) MEaSUREs InSAR-Based Antarctica Ice Velocity Map, Version 2. Boulder, Colorado USA. NASA National Snow and Ice Data Center Distributed Active Archive Center. doi: 10.5067/D7GK8F5J8M8R.
- Rignot E., Mouginot J. and Scheuchl B. (2011) Ice flow of the antarctic ice sheet. *Science* **333**, 1427–1430. <https://doi.org/10.1126/science.1208336>.
- Scherer P., Schultz L., Neupert U., Knauer M., Neumann S., Leya I., Michel R., Mokos J., Lipschutz M. E., Metzler K., Suter M. and Kubik P. W. (1997) Allan Hills 88019: an Antarctic H-chondrite with a very long terrestrial age. *Meteorit. Planet. Sci.* **32**, 769–773.
- Schultz L., Annestad J. O. and Delisle G. (1990) Ice movement and mass balance at the Allan Hills Icefield. *Antarct. J. United States* **25**, 94–95.
- Seddik H., Greve R., Zwinger T., Gillet-Chaulet F. and Gagliardini O. (2012) Simulations of the Greenland ice sheet 100 years into the future with the full Stokes model Elmer/Ice. *J. Glaciol.* **58**, 427–440. <https://doi.org/10.3189/2012JoG11J177>.
- Sharma P., Kubik P. W., Fehn U., Gove H. E., Nishiizumi K. and Elmore D. (1990) Development of <sup>36</sup>Cl standards for AMS. *Nucl. Instrum. Methods Phys. Res. B* **52**, 410–415.
- Shimizu H., Masuda A. and Tanaka T. (1983) Cerium anomaly in REE pattern of Antarctic eucrite. *Mem. Natl. Inst. Polar Res.* **30**, 341–348.
- Sinisalo A., Grinsted A., Moore J. C., Meijer H. A. J., Martma T. and van de Wal R. S. W. (2007) Inferences from stable water isotopes on the Holocene evolution of Scharffenbergbotnen blue-ice area, East Antarctica. *J. Glaciol.* **53**, 427–434. <https://doi.org/10.3189/002214307783258495>.
- Sinisalo A. and Moore J. C. (2010) Antarctic blue ice areas (BIAs) – towards extracting paleoclimate information. *Antarct. Sci.* **22**, 99–115. <https://doi.org/10.1053/j.semperi.2014.07.001>.
- Spaulding N. E., Higgins J. A., Kurbatov A. V., Bender M. L., Arcone S. A., Campbell S., Dunbar N. W., Chimiak L. M., Introne D. S. and Mayewski P. A. (2013) Climate archives from 90 to 250 ka in horizontal and vertical ice cores from the Allan Hills blue ice area, Antarctica. *Quat. Res.* **80**, 562–574. <https://doi.org/10.1016/j.yqres.2013.07.004>.
- Spaulding N. E., Spikes V. B., Hamilton G. S., Mayewski P. A., Dunbar N. W., Harvey R. P., Schutt J. and Kurbatov A. V. (2012) Ice motion and mass balance at the Allan Hills blue-ice area, Antarctica, with implications for paleoclimate reconstructions. *J. Glaciol.* **58**, 399–406. <https://doi.org/10.3189/2012JoG11J176>.
- Suganuma Y., Miura H., Zondervan A. and Okuno J. (2014) East Antarctic deglaciation and the link to global cooling during the Quaternary: evidence from glacial geomorphology and 10 Be surface exposure dating of the Sør Rondane Mountains, Dronning Maud Land. *Quat. Sci. Rev.* **97**, 102–120. <https://doi.org/10.1016/j.quascirev.2014.05.007>.
- Thiery W., Gorodetskaya I. V., Bintanja R., van Lipzig N. P. M., van den Broeke M. R., Reijmer C. H. and Kuipers Munneke P. (2012) Surface and snowdrift sublimation at Princess Elisabeth station, East Antarctica. *Cryosph.* **6**, 841–857. <https://doi.org/10.5194/tc-6-841-2012>.
- Touzeau A., Landais A., Stenni B., Uemura R., Fukui K., Fujita S., Guilbaud S., Ekaykin A., Casado M., Barkan E., Luz B., Magand O., Teste G., Meur E. L., Baroni M., Savarino J., Bourgeois I. and Risi C. (2016) Acquisition of isotopic composition for surface snow in East Antarctica and the links to climatic parameters. *The Cryosphere* **10**, 837–852. <https://doi.org/10.5194/tc-10-837-2016>.
- Uglietti C., Zapf A., Jenk T. M., Sigl M., Szidat S., Salazar G. and Schwikowski M. (2016) Radiocarbon dating of glacier ice: overview, optimisation, validation and potential. *The Cryosphere* **10**, 3091–3105. <https://doi.org/10.5194/tc-10-3091-2016>.
- van As D., van den Broeke M. R. and Helsen M. M. (2007) Strong-wind events and their impact on the near-surface climate at Kohnen Station on the Antarctic Plateau. *Antarct. Sci.* **19**, 507–519. <https://doi.org/10.1017/S095410200700065X>.
- van den Broeke M., König-Langlo G., Picard G., Kuipers Munneke P. and Lenaerts J. (2010) Surface energy balance, melt and sublimation at Neumayer Station, East Antarctica. *Antarct. Sci.* **22**, 87–96. <https://doi.org/10.1017/S0954102009990538>.
- van den Broeke M., Reijmer C., van As D. and Boot W. (2006) Daily cycle of the surface energy balance in Antarctica and the influence of clouds. *Int. J. Climatol.* **26**, 1587–1605. <https://doi.org/10.1002/joc.1323>.
- Van Ginneken M., Genge M. J. and Harvey R. P. (2018) A new type of highly-vaporized microtektite from the Transantarctic Mountains. *Geochim. Cosmochim. Acta* **228**, 81–94. <https://doi.org/10.1016/j.gca.2018.02.041>.
- Van Liefferinge B. and Pattyn F. (2013) Using ice-flow models to evaluate potential sites of million year-old ice in Antarctica. *Clim. Past* **2335–2345**, 2335–2345. <https://doi.org/10.5194/cp-9-2335-2013>.



- Van Liefvering B., Pattyn F., Cavitte M. G. P., Karlsson N. B., Young D. A., Sutter J. and Eisen O. (2018) Promising Oldest Ice sites in East Antarctica based on thermodynamical modelling. *The Cryosphere*.
- van Wessem J. M., Reijmer C. H., Morlighem M., Mouginit J., Rignot E., Medley B., Joughin I., Wouters B., Depoorter M. A., Bamber J. L., Lenaerts J. T. M., van de Berg W. J., van den Broeke M. R. and Van Meijgaard E. (2014) Improved representation of East Antarctic surface mass balance in a regional atmospheric climate model. *J. Glaciol.* **60**, 761–770. <https://doi.org/10.3189/2014JoG14J051>.
- Weigel A., Eugster O., Koeberl C. and Krähenbühl U. (1997) Differentiated achondrites Asuka 881371, an angrite, and Divnoe: Noble gases, ages, chemical composition, and relation to other meteorites. *Geochim. Cosmochim. Acta* **61**, 239–248. [https://doi.org/10.1016/S0016-7037\(96\)00341-9](https://doi.org/10.1016/S0016-7037(96)00341-9).
- Welten C., Alderliesten C., van der Borg K., Lindner L., Loeken T. and Schultz L. (1997) Lewis Cliff 86360: an antarctic L-chondrite with a terrestrial age of 2.35 million years. *Meteorit. Planet. Sci.* **32**, 775–780.
- Welten K. C., Folco L., Nishiizumi K., Caffee M. W., Grimberg A., Meier M. M. M. and Kober F. (2008) Meteoritic and bedrock constraints on the glacial history of Frontier Mountain in northern Victoria Land, Antarctica. *Earth Planet. Sci. Lett.* **270**, 308–315.
- Welten K. C., Nishiizumi K., Caffee M. W., Hillegonds D. J., Johnson J. A., Julli A. J. T., Wieler R. and Folco L. (2006) Terrestrial ages, pairing, and concentration mechanism of Antarctic chondrites from Frontier Mountain, Northern Victoria Land. *Meteorit. Planet. Sci.* **41**, 1081–1094. <https://doi.org/10.1111/j.1945-5100.2006.tb00506.x>.
- Whillans I. M. and Cassidy W. a. (1983) Catch a falling star: meteorites and old ice. *Science* **222**, 55–57. <https://doi.org/10.1126/science.222.4619.55>.
- Winter K., Woodward J., Dunning S. A., Turney C. S. M., Fogwill C. J., Hein A. S., Golledge N. R., Bingham R. G., Marrero S. M., Sugden D. E. and Ross N. (2016) Assessing the continuity of the blue ice climate record at Patriot Hills, Horseshoe Valley, West Antarctica. *Geophys. Res. Lett.* **43**, 2019–2026. <https://doi.org/10.1002/2015GL066476>.
- Yanai K. (1978) First meteorites found in Victoria Land, Antarctica, December 1976 and January 1977. *Mem. Natl. Inst. Polar Res.* **8**, 51–69.
- Yanai K., Kojima H. and Naraoka H. (1993) The Asuka-87 and Asuka-88 collections of Antarctic meteorites: search, discoveries, initial processing, and preliminary identification and classification. *Proc. NIPR Symp. Antarct. Meteorites* **6**, 137–147.
- Yoshida M., Ando H., Omoto K., Naruse R. and Ageta Y. (1971) Discovery of Meteorites near Yamato Mountains, East Antarctica. *Antarct. Rec.* **39**, 62–65.
- Zekollari H. (2017) TopoZeko: A MATLAB function for 3-D and 4-D topographical visualization in geosciences. *SoftwareX* **6**, 285–292. <https://doi.org/10.1016/j.softx.2017.10.004>.
- Zekollari H., Huybrechts P., Noël B., van de Berg W. J. and van den Broeke M. R. (2017a) Sensitivity, stability and future evolution of the world's northernmost ice cap, Hans Tausen Iskappe (Greenland). *Cryosph.* **11**, 805–825. <https://doi.org/10.5194/tc-11-805-2017>.
- Zekollari H., Lecavalier B. S. and Huybrechts P. (2017b) Holocene evolution of Hans Tausen Iskappe (Greenland) and implications for the palaeoclimatic evolution of the high Arctic. *Quat. Sci. Rev.* **168**, 182–193. <https://doi.org/10.1016/j.quascirev.2017.05.010>.
- Zolensky M., Bland P., Brown P. and Halliday I. (2006) Flux of extraterrestrial materials. *Meteorites Early Sol. Syst.* **II**, 869–888. [https://doi.org/10.1016/0304-8853\(96\)00112-6](https://doi.org/10.1016/0304-8853(96)00112-6).
- Zwinger T., Malm T., Schäfer M., Stenberg R. and Moore J. C. (2015) Numerical simulations and observations of the role of katabatic winds in the creation and maintenance of Scharffenbergbotnen blue ice area Antarctica. *The Cryosphere* **9**, 1415–1426. <https://doi.org/10.5194/tc-9-1415-2015>.

Associate editor: Christian Koeberl